Quaternary Science Reviews xxx (xxxx) 106812

Contents lists available at ScienceDirect

Quaternary Science Reviews

journal homepage: http://ees.elsevier.com

Late Quaternary coastal uplift of southwestern Sicily, central Mediterranean sea

Ferranti Luigi [a,b,*], Burrato Pierfrancesco [b], Sechi Daniele [c], Andreucci Stefano [d], Pepe Fabrizio [e], Pascucci Vincenzo [c,f]

[a] Department of Earth Sciences, Environment and Resources (DiSTAR), University Federico II, Naples, Italy
[b] Istituto Nazionale di Geofisica e Vulcanologia (INGV), Rome, Italy
[c] Department of Architecture, Design and Planning, University of Sassari, Italy
[d] Department of Chemical and Geological Sciences, University of Cagliari, Italy
[e] Department of Earth and Sea Sciences (DiSTeM), University of Palermo, Italy
[f] Institute of Geology and Petroleum Technologies, Kazan Federal University, Kazan, RU, Russia

ARTICLE INFO

Article history:
Received 30 September 2020
Received in revised form 2 January 2021
Accepted 16 January 2021
Available online xxx
Handling Editor: I Hendry

Keywords
Marine terraces
Aeolian ridges
Luminescence dating
Pleistocene
Frontal thrust belt
Fold growth
Southwestern sicily
Mediterranean sea

ABSTRACT

Mapping and luminescence aging of raised marine terraces and aeolian ridges along an ~90 km coastal stretch in southwestern Sicily provide the first quantitative assessment of vertical tectonic deformation in this region, which spans the frontal part of an active thrust belt. We recognized a staircase of eleven terraces and nine related aeolian ridges. The elevation profile of terraces parallel to the coast shows a >90 km long bell-shaped pattern, onto which shorter-wavelength (~10 km long) undulations are superimposed. Luminescence ages from terraced beach deposits and aeolian sediments constrain the position of paleoshorelines formed during MIS 5e, 7a and 7c, with a maximum uplift rate of ~0.75 mm/a, and indicate a late Middle-Late Pleistocene (80–400 ka) age for the sequence of terraces. The elevation of Lower Pleistocene morpho-depositional markers points that uplift may have occurred at similar rates at the beginning of the Early Pleistocene, but almost zeroed between ~1.5 and 0.4 Ma before the recent renewal. The uneven elevation of Middle-Upper Pleistocene paleoshorelines observed moving along the coast documents that uplift embeds both a regional and a local component. The regional, symmetric bell-shaped uplift is related to involvement in the thrust belt of thicker crustal portions of the northern African continental margin. The short-wavelength undulations represent the local component and correspond to actively growing bedrock folds. The present study contributes to unravel the different spatial and temporal scales of deformation processes at a collisional margin.

1. Introduction

The analysis of displaced marine terraces along tectonically active coasts can provide fruitful insights into tectonic processes occurring at subduction (e. g., Plafker and Rubin, 1978; Jara-Muñoz et al., 2015), transform (e. g., Gurrola et al., 2014; Muhs et al., 2014) or collisional (e. g., Armijo et al., 1996) margins. Detailed geomorphological analysis, combined with geochronological constraints and models of coastal evolution, as this study show for the southwestern Sicily coast in the central Mediterranean, can afford an accurate quantification of the relative contribution of far-field and local tectonic sources to the net vertical displacement of the coast.

Within the central Mediterranean setting, controlled by the interaction between the Adriatic-African and European continental margins (inset in Fig. 1; e. g. Faccenna et al., 2001), several studies have used marine terraces to unravel the recent tectonic scenario. In southern Italy and Sicily, a generalized increase of uplift started around the Middle Pleistocene (e. g. Westaway, 1993; Miyauchi et al., 1994; Ferranti et al., 2006; 2009; Santoro et al., 2009 among others). Previous studies have shown that uplift was by far highest in Calabria and eastern Sicily compared to surrounding regions, possibly in relation to residual oceanic subduction of the steep Ionian slab beneath the Calabrian forearc (Fig. 1; Westaway, 1993; Ferranti et al., 2010; Faccenna et al., 2011).

Among the Pleistocene terraces observed in southern Italy, the ones attributed to the Marine Isotopic Stage (MIS) 5e stand as a prominent regional benchmark for coastal tectonics (Fig. 1; Bordoni and Valensise, 1998; Ferranti et al., 2006). In Sicily, a progressive westward and southward decrease in uplift rate of the MIS 5e shoreline is observed moving away from the northeastern tip of the island (Fig. 1; Antonioli et al., 2006). However, the pattern and time of vertical deformation along the southwestern coast of Sicily is basically unknown because no reliable constraints exist on the age of Pleistocene marine terraces in this area (Antonioli et al., 2006; D'Angelo and Vernuccio, 1996).

* Corresponding author. Department of Earth Sciences, Environment and Resources (DiSTAR), University Federico II, Naples, Italy.
E-mail address: lferrant@unina.it (F. Luigi)

https://doi.org/10.1016/j.quascirev.2021.106812
0277-3791/

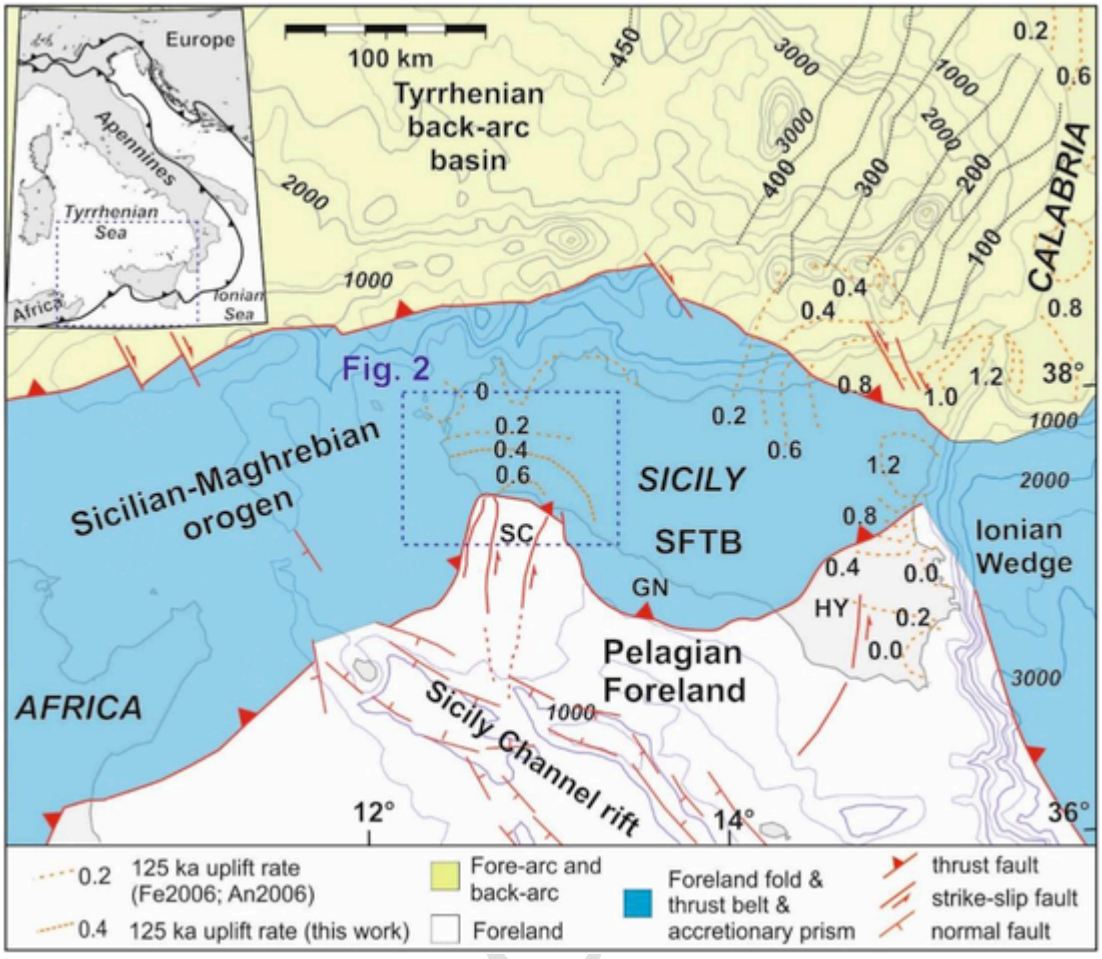

Fig. 1. Main tectonic features of the central Mediterranean area. Solid red lines are main faults (triangles on the up-thrust side of thrust faults, tick on hanging-wall side of normal fault). Dotted black lines are depth contours (km) to the Benioff-Wadati zone of the Ionian slab (after D'Agostino and Selvaggi, 2004). Orange lines are vertical deformation rates (mm/a) since the Late Pleistocene: after Ferranti et al., 2006-Fe2006, and Antonioli et al., 2006-An2006 (dashed); for southwestern Sicily, after this work (dotted). Water depth in m. Labels: GN, Gela Nappe; HY, Hyblean sector; SC, Saccense sector; SFTB, Sicily Fold and Thrust Belt. Inset show location of the figure in the tectonic context of the central Mediterranean; the thick solid lines are the main frontal thrust faults deforming the Adriatic-north African continental margin (triangles on the upper plate). Dashed rectangle indicates area enlarged in Fig. 2. (For interpretation of the references to color in this figure legend, the reader is referred to the Web version of this article.)

Southwestern Sicily spans the transition from the front of the Sicilian fold and thrust belt (SFTB) to the Pelagian foreland domain of northern Africa (Fig. 1). The thrust belt is thought to be currently moving along its basal thrust, although at relatively low displacement rate (Monaco et al., 1996; Lavecchia et al., 2007; Ferranti et al., 2008). The seismotectonic activity of this sector of Sicily is testified by the recurrent seismic destruction of the Selinunte Greek temples (Guidoboni et al., 2002; Bottari et al., 2009) and by the 1968 Belice seismic sequence (Fig. 2A; Azzaro et al., 2020, and references therein). Within this scenario, the coastal morphotectonic analysis may offer a substantial contribution to the understanding of active tectonic processes.

In this paper, we present the results of an integrated morpho-structural and geochronological analysis of the Upper Quaternary terraces cropping out in southwestern Sicily (Fig. 2A). By providing detailed age constraints and position for these ancient shorelines, the present study unveils the crustal deformation pattern of the region and contributes to a quantitative assessment of geodynamic models for the central Mediterranean.

2. Geological setting

2.1. Regional tectonic and seismotectonic frame

Southwestern Sicily is located on the frontal sector of the Maghrebian-Apennines orogenic belt, which, together with the Ionian accretionary wedge, forms the broad central-western Mediterranean collisional boundary between the African and the European plates (Fig. 1; Roure et al., 1990; Faccenna et al., 2001). The Sicilian segment of the orogen (Sicilian fold and thrust belt, SFTB) consists of a pile of thrust sheets developed at the expenses of paleogeographic domains of the Tethys ocean and of the north African continental margin (Bello et al., 2000; Catalano et al., 2000, 2013).

The foremost part of the SFTB indents around the Saccense and Hyblean sectors of the Pelagian foreland in the west and east, respectively (Fig. 1). These two foreland blocks are made of stiff Mesozoic-Cenozoic carbonate platform rocks, which acted as rigid salients and limited the forward propagation of the thrust front. Conversely, Mesozoic-Cenozoic basinal clays that are buried beneath central Sicily and its offshore, allowed greater southward advancement of the frontal thrust belt (Gela Nappe, Fig. 1) between the two foreland indenters (Lickorish et al., 1999; Ghisetti et al., 2009).

The frontal thrust belt submerged beneath the northwestern Sicily Channel (Adventure Thrust Front, Fig. 2A) steps onshore western

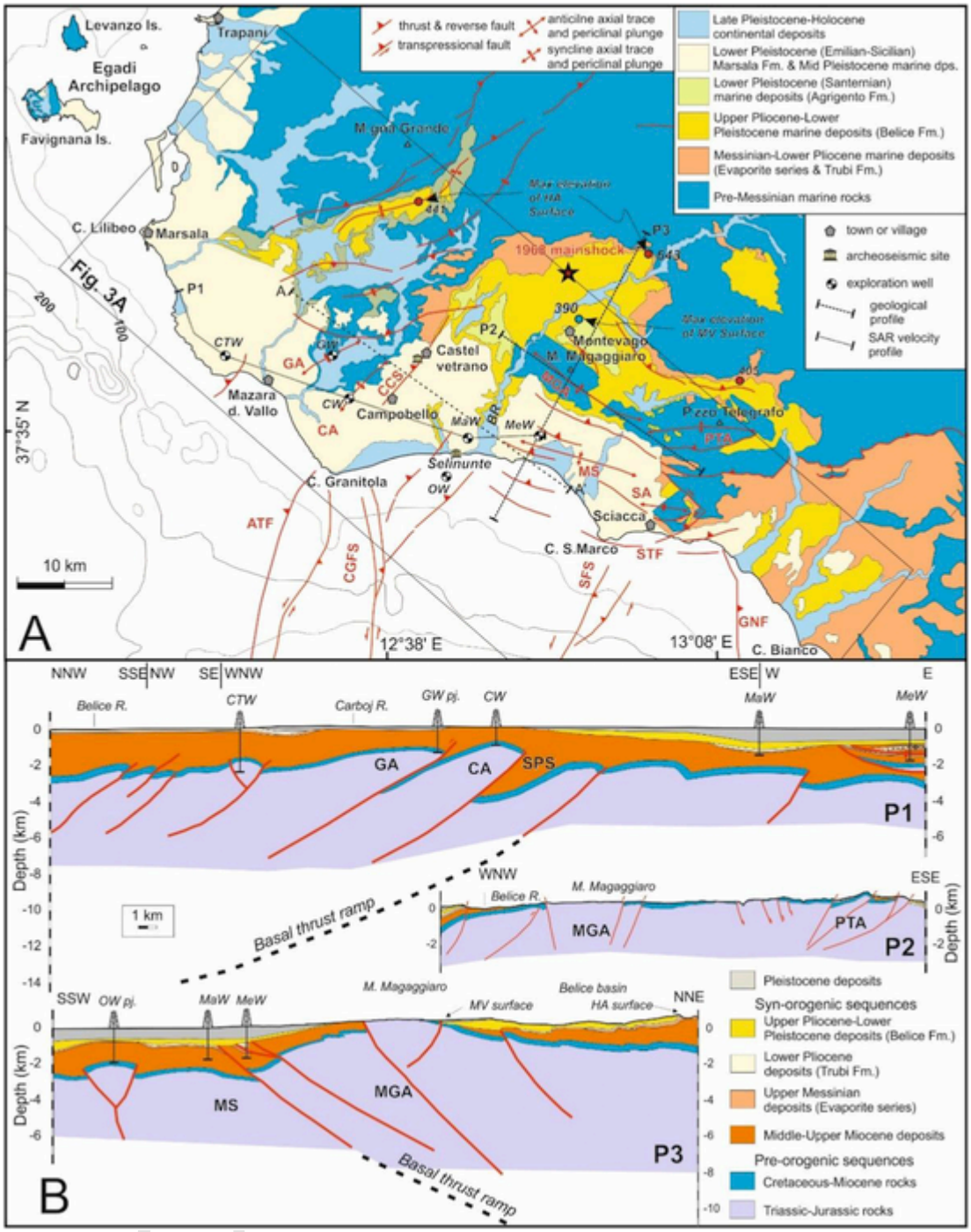

Fig. 2. – A) Tectonic map of southwestern Sicily (see Fig. 1 for location of area illustrated in this map). Geology from Lentini and Carbone (2014). Structures adapted and reinterpreted from Lentini and Carbone (2014), Montanari et al. (2017), Ferranti et al. (2019) (note that most thrust and reverse faults are buried). The epicentre of the mainshock of the 1968 Belice seismic sequence (star) is from CPTI15 (Rovida et al., 2021). The bathymetric metadata and Digital Terrain Model data products have been derived from the EMODnet Bathymetry portal - http://www.emodnet-bathymetry.eu (isobaths in m). P1 to P3 are the traces of profiles of Fig. 2B; A-A′ is the trace of SAR velocity profile of Fig. 15B. Erosional surfaces: MV, Montevago; HA, Highest Abrasional surface (maximum elevation in m indicated by dots). Structures: ATF, Adventure Thrust Front; CA, Campobello Anticline; CCS, Castelvetrano-Campobello Scarp; CGFS, Capo Granitola Fault System; GA, Gazzera Anticline; GNF, Gela Nappe Front; MGA, Magaggiaro Anticline; MS, Menfi Syncline; PTA, Pizzo Telegrafo Anticline; SFS, Sciacca Fault System; STF, Sciacca Thrust Front. Wells: CW, Campobello Well; CTW, Contrada Triglia Well; GW, Gazzera Well; MaW, Marinella Well; MeW, Menfi Well; OW, Onda Well. BR, Belice River. **B)** Geological profiles across southwestern Sicily, adapted and reinterpreted from: P1, Montanari et al. (2017); P2 and P3, Vitale (1990), Di Stefano and Vitale (1993). Basal thrust ramp drawn from Lavecchia et al. (2007). SPS, Selinunte Plain Syncline; other labels as in Fig. 2A.

Sicily where a system of NNE-SSW trending, east-verging thrust-ramp anticlines are developed in the Mesozoic-Cenozoic Trapanese pelagic carbonate platform and overlying Neogene cover strata (Campobello and Gazzera anticlines, Fig. 2A and B; Montanari et al., 2017 and references therein). North of Castelvetrano village, the frontal thrust belt turns to the east and merges with ~ESE-WNW trending, south-to southwest verging thrust structures in the Monte Magaggiaro and Pizzo Telegrafo ridges (Fig. 2A and B). These structures are thrust ramp anticlines, cored by thicker Mesozoic-Cenozoic carbonates of the Saccense platform (Fig. 2B). The foremost part of the belt forms an imbricate

fan whose tip is thought to emerge near the coastline (Sciacca thrust front; Fig. 2A). East of Sciacca, the frontal thrust structures step offshore and give way to the NNW-SSE striking front of the Gela Nappe (Figs. 1 and 2A).

The frontal thrust-fold system in southwestern Sicily developed during the Pliocene-Quaternary and is presently active, as highlighted by seismicity, geodesy and archeoseismic studies (Monaco et al., 1996; Bottari et al., 2009; Barreca et al., 2014, 2020). The forelimb of the Campobello anticline is expressed by a ~60 m tall scarp developed in Pleistocene deposits (CCS, Fig. 2A), and is characterized by archeoseismic and geodetic evidence of deformation (Barreca et al., 2014, 2020). Monaco et al. (1996) suggested that the Sciacca thrust anticline involves Upper Quaternary marine deposits and lacustrine sediments and was responsible for the 1968 Belice seismic sequence (mainshock $M_w = 6.4$, Fig. 2A).

Ahead of the thrust front, the offshore foreland domain is cut by the ~NNE-SSW trending Capo Granitola and Sciacca left-transpressional fault systems (Fig. 2A; Fedorik et al., 2017; Civile et al., 2018; Ferranti et al., 2019). Significant displacement on the deep-seated transcurrent faults mostly occurred during the Pliocene-Early Pleistocene but decreased substantially afterwards (Ferranti et al., 2019).

2.2. Overview of quaternary stratigraphy and terraces

The southwestern Sicily landscape consists in a gently sloping coastal plain floored by Quaternary deposits and locally by older rocks (Fig. 2A). Marine calcarenites and sands of the Agrigento Formation (Lower Pleistocene Santernian substage, ~1.8–1.5 Ma) are found in scattered patches in the more inland parts. In contrast, Lower Pleistocene (Emilian p. p.-Sicilian substages, ~1.5–0.8 Ma) marine deposits form a continuous blanket around the coast of western Sicily (Fig. 2A). They chiefly consist of bioclastic calcarenites and calcirudites (Marsala Calcarenite: Ruggieri et al., 1975; D'Angelo and Vernuccio, 1996; Di Maggio et al., 2009) in the west, which gradually pass to silty clays in the southeast and on the continental shelf (Ferranti et al., 2019). The stratigraphic architecture of these deposits features a prograding system developed in a wave-dominated shoreface setting (Di Maggio et al., 2009).

A regional-scale abrasion surface, traditionally known as Grande Terrazzo Superiore (GTS), "Great Upper Terrace", is carved on top of the Marsala Calcarenite (Ruggieri and Unti, 1974; Ruggieri et al., 1975). Development of the GTS is correlated with the beginning of the Middle Pleistocene (D'Angelo and Vernuccio, 1996), but its width and variable elevation suggest a polycyclic origin. A surface higher than the GTS, here labelled the Montevago surface, is perched at ~400 m on the northern flank of the M. Magaggiaro anticline in the east, where it levels deposits of the Agrigento Formation (Fig. 2A; 2B, profile P3). Further inland, remains of older abrasion surfaces carved in Pliocene-Lowermost Pleistocene deposits are mapped up to an elevation of ~650 m (Highest Abrasion surface, Fig. 2A; 2B, profile P3; Antonioli et al., 2006).

The Middle-Late Pleistocene Series includes a flight of marine terraces. Seven terrace orders have been identified by D'Angelo and Vernuccio (1996) at elevations ranging between 3 and 100 m above sea level (a.s.l.). These terraces are mainly represented by abrasion platforms, which are locally overlain by paleosols and by a thin cover of shallow-water deposits overlain by aeolian dunes (D'Angelo and Vernuccio, 1996). Through correlation between the relative position of terraces and isotope-based curves of eustatic sea level change, D'Angelo and Vernuccio (1996) attributed the seven terraces to MISs from 5e (~125 ka) to 15 (~600 ka), and the GTS to isotopic stage 17 (~700 ka). Their scheme is benchmarked on the correlation of their lowermost terrace with the MIS 5e shoreline, based on the reported finding (Ruggeri and Unti, 1974) from this terrace sediments of specimens of *Strombus bubonius* (LMK) (today identified as *Strombus (=Persististrombus) latus* GMELIN; Nalin et al., 2012, with references), an index fossil for the MIS 5e in the Mediterranean region. However, other authors (Ruggieri and Unti; 1974; Antonioli et al., 2006) attribute the fossiliferous deposits with *Persististrombus* to a terrace extending from the coast to an inner margin at ~30–40 m elevation, which they identify as the MIS 5e shoreline.

Moving inland, Quaternary deposits unconformably cover older rocks (Fig. 2A). Upper Pliocene-Lower Pleistocene sandstone, clays and calcarenites (Belice Marnoso-Arenacea Formation; Ruggieri et al., 1975; Vitale, 1990) are exposed below the Marsala Calcarenites and the Agrigento Formation. These sediments were deposited within a deltaic-turbiditic setting controlled by active growth of basement folds (Vitale, 1990). Older rocks outcropping in the coastal belt are Lower Pliocene pelagic marl and calcilutite (Trubi Formation), the Upper Messinian evaporite series deposited during the Mediterranean-wide salinity crisis (Malinverno et al., 1981), and Middle-Upper Miocene terrigenous deposits (Fig. 2A and B).

In several cases, river incision and denudation processes dismantled the more resistant Marsala Calcarenites and unearthed easily erodible pre-Quaternary rocks below. By these means, relief inversion processes produced synclinal ridges and anticlinal valleys (Di Maggio et al., 2017) as in the case of the Gazzera anticline (Fig. 2A).

3. Methods

3.1. Mapping

We integrated field and remote sensing techniques to map the Middle-Upper Pleistocene morpho-depositional units that include depositional terraces and abrasion platforms, and linear aeolian ridges, within an area that extends ~90 km parallel to the coastline between Capo Lilibeo near Marsala in the west and Capo Bianco in the east (Fig. 3A). The study area was divided in a western, a central and an eastern sector based on morphology and elevation pattern of terraces and aeolian ridges (Fig. 3B). We studied in higher detail the western and most of the central sectors, where the terrace flight is more complete (Fig. 4A). Within these latter sectors, detailed stratigraphic observations were carried out at twenty-seven natural exposures (Table S1) to characterize terrace and aeolian ridge deposits.

We distinguished eleven orders of marine terrace (T1-T11) and ten orders of dune ridges (D1-D10; Figs. 3A and 4A). Because of limited erosional or depositional modification of these features after their formation, they are generally well preserved in the present landscape of southwestern Sicily. Only along the entrenched course of coastal rivers the terraces have been erased by the intense regressive fluvial erosion (Figs. 3A and 4A).

The morpho-depositional units were mapped integrating field observations with aerial photogrammetry and Digital Elevation Model (DEM) analysis. We used a dataset of 1/33k scale air photos taken in 1953/1954 to draw a preliminary GIS map of the morphological features that was then checked using topographic profiles, contour at 1 m spacing and slope map analysis from a LiDAR digital surface model with a 2 m resolution downloaded from the Regione Sicilia web site (http://www.sitr.regione.sicilia.it/). The position of morphological features was then sample checked through ground truthing during field work. We estimate a maximum positioning plus elevation uncertainty of 5 m.

Inner margins of marine terraces typically stand in the field as small steps in the gently sloping coastal plain, and they were traced with variable continuity on aerial photographs and on the DEM. More or less extensive abrasion platform remnants carved on the Marsala Calcarenite are genetically associated to terraces and were mostly observed in the western part of the study area (Fig. 4A). Elongated linear ridges representing aeolian dunes are widespread and are well delineated both in the field and in remote images (Fig. 4A).

We used both the elevation of inner margins and the facies of terraced marine deposits to establish the present day elevation of the paleoshorelines. We applied bathymetric corrections (see Pascucci et al.,

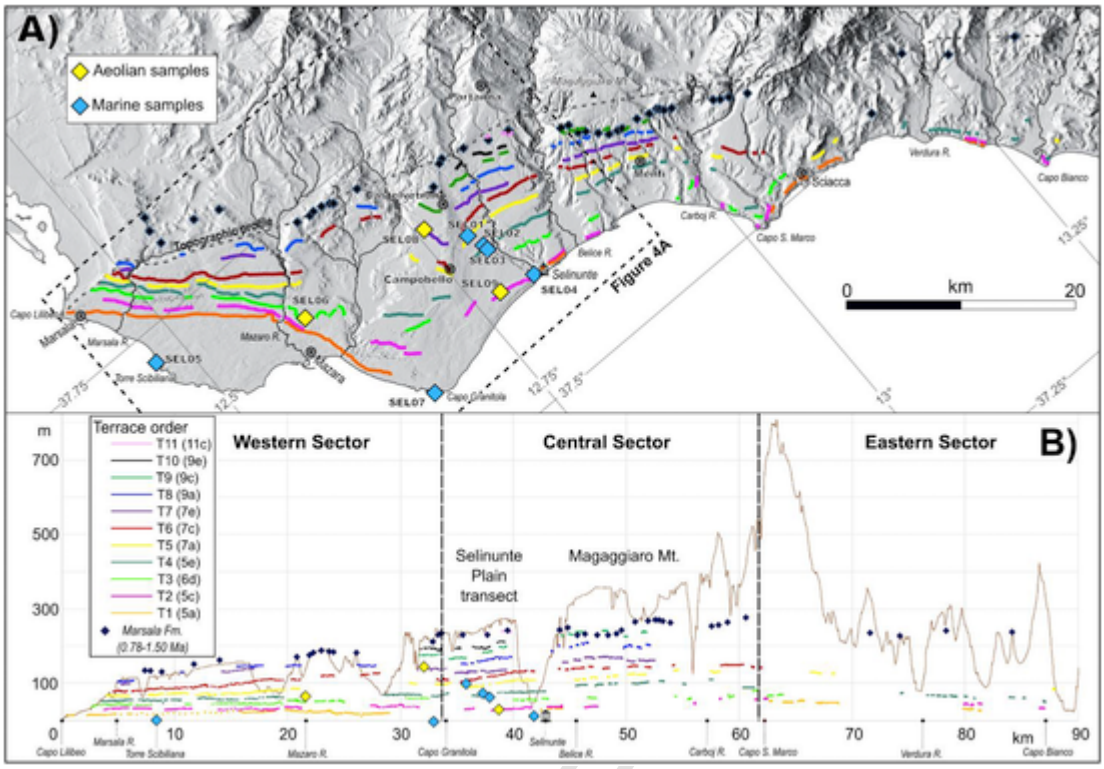

Fig. 3. A) Map of southwestern Sicily showing the inner margins of marine terraces T1-T11 and the innermost position of outcrops of the Marsala Calcarenite. The attribution of marine terraces to Marine Isotopic Stages is indicated in parenthesis beside the terrace order. The dashed rectangle encloses the area shown in Fig. 4A. **B)** projection of terraces inner margins and of Marsala Calcarenite innermost outcrops elevation onto a N135 striking profile (horizontal reference line for the rotated map). The solid line is the topographic profile (trace in Fig. 3A). Diamonds labelled SEL01 to SEL08 indicate position of luminescence samples (map location in Figs. 3A and 4A). The figure shows the subdivision of study area in western, central and eastern sectors, and the schematic location of the Selinunte plain and M. Magaggiaro transects used for computation of uplift rates (see Fig. 12 and 14).

2018; 2019; Hamon-Kerivel et al., 2020) to the logged deposits depending on the observed facies association (see Table S1 for the interpretation of the lithofacies in terms of depositional environment and for the adopted corrections). In general, marine deposits and abrasion platforms were assigned to the nearest overlying inner margin. The elevation of the sedimentary section corrected for the estimated paleo-bathymetry was generally found to match and, in many cases was used, to refine the paleoshoreline position estimated on the base of the inner margin elevation.

3.2. Luminescence analysis

Deposits from marine terraces and aeolian ridges were sampled and dated using both quartz, through Optically Stimulated Luminescence (OSL), and k-feldspar, through Infra-Red Stimulated Luminescence (IRSL) and post-IR IRSL measured at 290 °C (pIRIR290) methods (Pascucci et al., 2014; Andreucci et al., 2017; Casini et al., 2020; Sechi et al., 2020). Marine samples were taken at the shoreface/foreshore boundary to minimize the bathymetric correction. This boundary is used as a paleo-sea level marker because, in the Mediterranean Sea, it is normally placed at 0 ± 30 cm relative to the present sea level (Pascucci et al., 2018, 2019).

3.2.1. Sample collection, preparation, and facilities

Nine samples (SEL01 to SEL09) were collected for luminescence dating (locations in Figs. 3A and 4A) and were taken from moderately cemented sandstone with mixed carbonate-quartz cement. They were sampled as blocks (40 × 40 × 40 cm) and sealed in black plastic bags to avoid further exposition to sunlight. Blocks were treated at the Luminescence dating laboratory of the University of Sassari under subdued red light. The outer part of each block (5 cm of thickness) was removed to discard material possibly exposed to light during sampling. This outer material was stored and used for water content and dose rate (Dr) analysis. The inner part was treated following the standard procedures for sand-sized samples (Porat et al., 2015). For all samples, the 90–180 μm grain-size fraction of quartz and K-feldspar grains was chosen for luminescence dating. Samples SEL04 and SEL05 did not provide enough quartz and K-feldspar grains to obtain a reliable luminescence age. From sample SEL03, only quartz grains were sufficiently abundant for further analysis.

The quartz and K-feldspar grains were mounted as multi-grain small aliquots (approximately 200 grains) on stainless steel discs of 9.7 mm in diameter and 0.2 mm in thickness using silicon spray as adhesive. All luminescence measurements were performed using two Risø TL/OSL-DA-20 readers provided with different calibrated sources (0.2343 and 0.1168 Gy/s) of beta radiations 90Sr/90Y (Bøtter-Jensen et al., 2010). Quartz grains were stimulated with blue LEDs for 40 s at 125 °C and OSL signal was detected through a 7.5 mm Hoya U-340 filter, while infrared LEDs were used for stimulation of K-feldspar grains and the luminescence signal was detected through a combination of Schott BG39 and Corning 7–59 filters.

3.2.2. Dose rate measurement

Dose rates (Dr) were calculated combining data measured with Inductively Coupled Plasma Mass Spectrometry (ICP-MS) and Low-level beta GM multicounter system model Risø GM-25-5 (Bøtter-Jensen and Mejdahln, 1988). The nine collected samples show similar depositional characteristics and source area. They could therefore be considered similar from a petrographic and sedimentological point of view. Thus, the most representative samples (SEL03, SEL05, SEL06, SEL07) were measured with ICP-MS to obtain the concentration of Uranium, Thorium and Potassium (Table 1) and, subsequently element concentrations were converted in total dry Dr (Gy/ka) using the conversion factor of Guèrin et al. (2011). The dose rate of samples (SEL01,

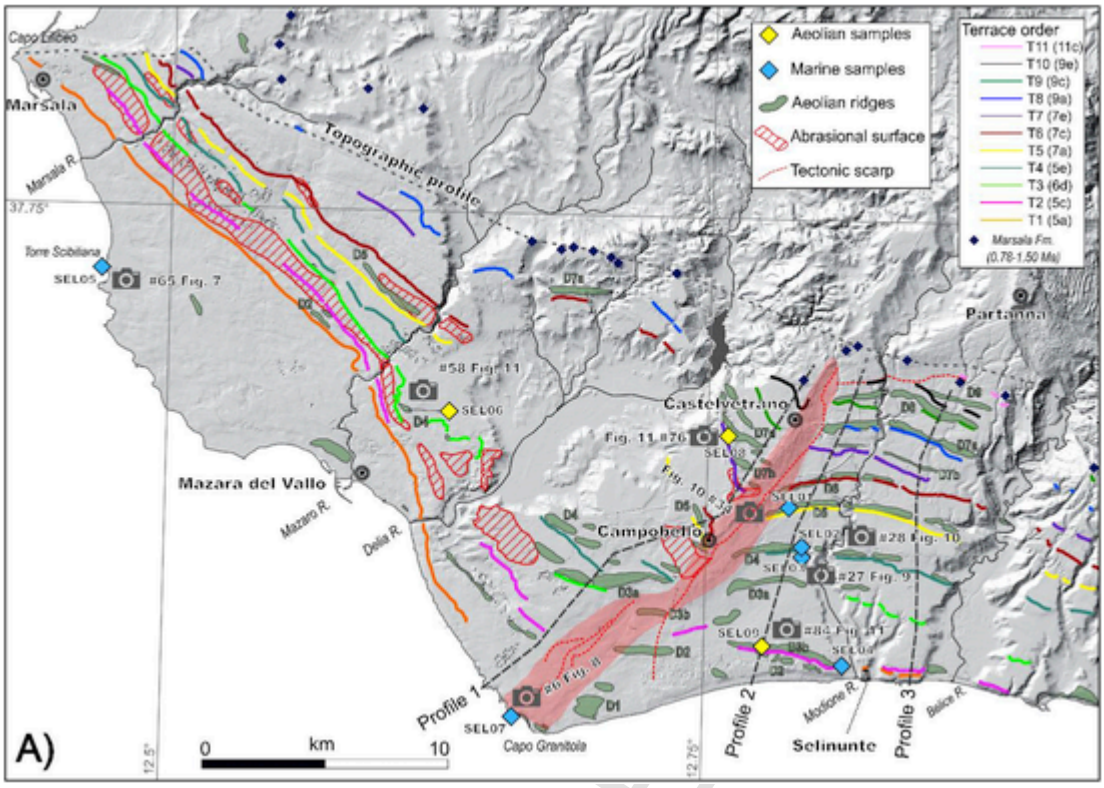

Fig. 4. AA) Map of the western and central sectors of southwestern Sicily, showing the inner margins of marine terraces T1-T11 and associated abrasion surfaces, the aeolian ridges D1-D10, and the innermost position of the Marsala Calcarenite outcrops. The attribution of marine terraces to Marine Isotopic Stages is indicated in parenthesis beside the terrace order. Diamonds labelled SEL01 to SEL08 indicate position of luminescence samples. Dashed lines are traces of topographic profiles 1, 2, 3 shown in Fig. 4B. Location of stratigraphic logs and pictures shown in Fig. 7–11 is indicated. 4B (*continued*) – B) Topographic profiles roughly perpendicular to the coastline showing the flight of marine terraces and associated aeolian ridges in the Castelvetrano-Granitola Ridge (western sector) (profile 1) and in the western (profile 2) and eastern (profile 3) Selinunte Plain (central sector). Italic numbers below the profiles list the local elevation of inner margins. Terrace orders are color-coded according to colors used in Fig. 4A. The slope % value along each profile is reported below them. Prominent spikes in most cases highlight the location of inner margin and associated riser dunes. Traces of profiles are in Fig. 4A. (For interpretation of the references to color in this figure legend, the reader is referred to the Web version of this article.)

SEL02, SEL04, SEL08, SEL09) has been estimated with the beta counter (Cunningham et al., 2018). For all samples, the dry dose rate was corrected for moisture attenuation determined in the laboratory. The averaged water content of completely dry and saturated material normalized for the field saturation is considered as the life-time water content during burial time (Table 2). An absolute uncertainty of ±4% was assumed based on this procedure. Attenuation factor due to the grain size on beta dose rate was applied (Guèrin et al., 2012) and the contribution of cosmic rays to the final dose-rate was calculated after Prescott and Hutton (1994). Moreover, the contribution of internal ^{4} K to the final K-feldspar (90–180 μm) grains Dr was calculated assuming 12.5 ± 0.5% of the total weight of K, and Rb concentration of 400 ± 100 ppm (Huntley and Baril 1997). All dose-rate information is presented in Table 2.

3.2.3. Luminescence characteristics

The conventional single-aliquot regenerative dose (SAR) protocol was applied to calculate the equivalent dose (De) of quartz samples (Murray and Wintle, 2000, 2003). The presence of feldspar IRSL response on OSL quartz net signal was tested using IR-depletion test (Duller et al., 2003). All samples show a negligible IRSL feldspar contribution (<10% of unity). In order to determine the most appropriate thermal treatment to be adopted during the SAR protocol a dose recovery preheat plateau test was applied on sample SEL07. Twenty-four aliquots were bleached twice inside the Risø TL/OSL-DA-20 reader at room temperature with blue light stimulation separated by a pause of 10 ks to let traps to recombine. An administered known dose of ~118 Gy was given to all aliquots and measured at eight different temperatures of preheat from 180 to 320 °C, with three aliquots being measured at each temperature (Fig. 5A). The cutheat temperature was set 20 °C lower than the respective preheat temperature (Roberts, 2006). A dose recovery preheat plateau between 180 °C and 320 °C was observed and the measured/given dose (dose recovery) ratio is 0.99 ± 0.02 on average (Fig. 5A). Thus, the SAR protocol for the nine samples was set with temperatures of 260 °C for preheat, 240 °C for cutheat and a clean-out at the end of each SAR cycle at 280 °C for 40 s.

At least 24 aliquots were analyzed for equivalent dose (De) determination. The dose response curve was always fitted with a single saturating exponential function. The early background method was applied and the first 0.72 s of the stimulation curve used for OSL signal integration, after subtracting the background signal derived from the subsequent 0.72–2.9 s integral to minimize contamination from the medium and slow components (Cunningham and Wallinga, 2010). Samples show bright quartz signal and a fast-component dominated decay shine-down curve, except for samples SEL 04 and SEL05 that show no or extremely dim natural signals. Thus, SEL04 and SEL05 were not considered further for dating. A decay and a dose response curve for sample SEL03 are shown in figure Fig. 5B. Recuperation and recycling ratios based on all measured aliquots are in average 0.98 ± 0.003 and 0.04 ± 0.01% (on natural signal) respectively (Fig. 5C and D). To confirm reliability and reproducibility of the SAR protocol, a dose recovery test was performed on samples SEL03 and SEL09. Ten aliquots for each sample were sunlight bleached for 10 Sardinian sunny days, and an administered known dose of 80 Gy was given before any thermal treatment. The derived equivalent doses were calculated using the SAR protocol set with the above determined parameters. The average dose re-

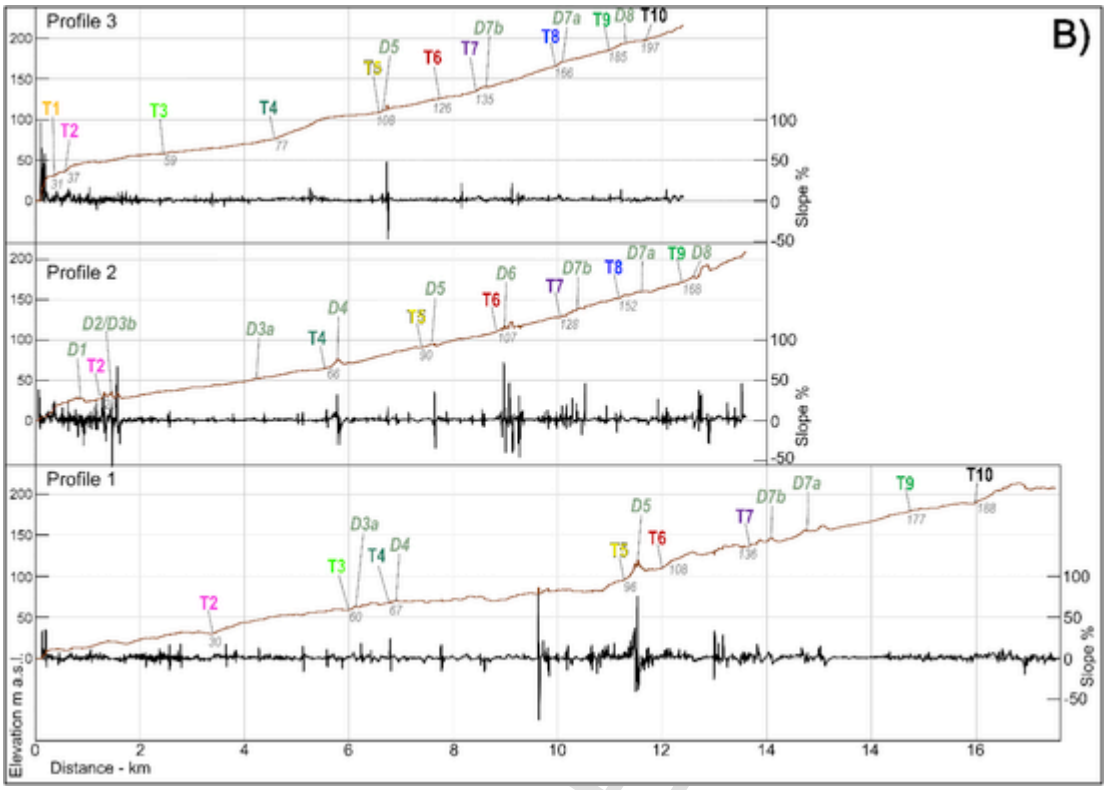

Fig. 4. *Continued*

Table 1
ICP-MS concentrations of elements for measured samples.

Sample	K (%)^	±	U (ppm)	±	Th (ppm)	±
SEL03	0.07	0.01	0.7	0.1	0.7	0.01
SEL05	0.10	0.01	0.6	0.1	1.0	0.01
SEL06	0.06	0.01	0.9	0.1	1.2	0.01
SEL07	0.15	0.01	0.7	0.1	1.5	0.01

^% of the total weight of K.

covery ratio based on all the measured aliquots is of about 0.96 ± 0.02 (Fig. 6A). Thus, the protocol is considered suitable for dating those samples.

The natural signal saturation limits (not greater than 85% of 2Do) of quartz grains was used as a rejection criterion and only those aliquots with saturation value (2Do) greater than the average equivalent dose (De, derived from all aliquots) were used for final sample De determinations and the derived *"true"* ages are considered reliable (Thomsen et al., 2016; Yi et al., 2016). Conversely, samples showing a natural luminescence signal close or beyond the limit of laboratory saturation (>85% of 2Do) cannot be used for *"true"* age determinations. However, using as final equivalent dose the derived 2Do, a minimum age can be calculated (Wintle and Murray, 2006; Robert et al., 2008). The other standard rejection criteria for measured aliquots were recycling and recuperation (Wintle and Murray, 2006). Table 2 summarizes the resulting final De values along with *"true"* and minimum quartz SAR-OSL ages.

A $pIRIR_{225}$ protocol was employed for K-feldspar analysis (Buylaert et al., 2009; Thiel et al., 2011) with a preheat temperature at 250 °C and a pIRIR stimulation at 225 °C (pIRIR225) for 200 s after a IR at 50 °C stimulation for 200 s. During the routine analysis test dose was kept around 50% of natural dose in order to avoid underestimation of De value (Li et al., 2014; Lui et al., 2016; Yi et al., 2016; Colarossi et al., 2018; Carr et al., 2018). The initial 2 s of pIRIR signals were subtracted by the last 50 s of the respective signals to determine the signal intensity. Dose response curve was fit with a single exponential function. At least 20 aliquots for each samples were measured. The dose response and $pIRIR_{225}$ natural shine-down decay curves signal of sample SEL 01 are shown in Fig. 6B. Recycling and recuperation ratios based on all the measured aliquots are 0.996 ± 0.001 and 0.048 ± 0.03% respectively (Fig. 6C and D). Dose recovery test and residual dose (RD) measurements were conducted to evaluate the suitability and reproducibility of pIRIR protocol. Twelve aliquots for all samples were naturally bleached for ten Sardinian sunny days. Six aliquots were used to measure the amount of unbleachable residual dose (RD; Kars et al., 2014; Andreucci et al., 2017) and listed in Table 2. The other six aliquots were utilized for dose recovery test and an administered beta dose of ~160 Gy was given prior to any thermal treatment and then the equivalent doses were measured using the $pIRIR_{225}$ protocol. To each sample, the measured residual dose was subtracted from the derived average De value and subsequently the dose recovery ratio was calculated. The average dose recovery ratio based on all measured aliquots is 0.96 ± 0.01 (Fig. 6D). Altogether, these results demonstrate that the $pIRIR_{225}$ protocol is suitable for dating the collected samples.

Six aliquots for each sample were used to quantify the athermal signal loss during time (fading) according to Auclair et al. (2003) using 2 days storage times. Fading rate (g_{2days}, %/decade of time) was determined following Huntley and Lamothe (2001). As expected, the fading rates are relatively low for all samples (g_{2days}-values < 2%/decade; Table 2). Despite the fact that the fading-uncorrected and the fading-corrected ages are in general within the errors of both (Table 2) we decide to use as final "*true*" ages the fading-corrected ones because better representative of the natural behavior of the K-feldspar grains through time.

Table 2
- Equivalent doses and associated age estimates for K-feldspar pIRIR225 quartz SAR. (WC) moisture expressed in percentage, (n) number of aliquot measured to estimate the palaeodose, (Sat): level of saturation of signal, (De) natural equivalent dose palaeodose, (OD) overdispersion of palaeodose measured, (Dr) environmental dose rate, (RD) residual dose, g2days (fading g-value). (a): paleodose estimated on 2Do, (b): minimum age calculated on 85% of 2Do, (#) feldspar ages corrected for fading. Sample SEL04 has not detectable signal. Sample SEL05 yielded insufficient feldspar material for dating. Final ages in last column are the selected ages. See text for details.

			Quartz SAR-OSL						K-feldspar pIRIR225							
Sample Code	Depth (cm)*	wc %	n	Sat	De (Gy)	OD (%)a	Dr tot (Gy/ka)#	Q-Age (ka)	n	De (Gy)	RD (Gy)	g2days (%/dec)	Dr tot (Gy/ka)#	Age (ka)	Age# (ka)	Preferred Age (ka)
SEL01	100	8.2	5	yes	123a	–	0.56 ± 0.04	220b	19/22	210 ± 3	5.7 ± 1.6	1.2 ± 0.1	1.02 ± 0.03	200 ± 7	218 ± 8	218 ± 8
SEL02	100	9.9	5	yes	86a	–	0.63 ± 0.04	136b	19/21	208 ± 2	7.1 ± 2.8	1.19 ± 0.07	1.09 ± 0.03	184 ± 6	200 ± 7	200 ± 7
SEL03	100	2.8	28/31		70 ± 4	29	0.56 ± 0.04	125 ± 11	–	–	–	–	–	–	–	125 ± 11
SEL04	100	12.2	4	ns	–	–	–	–	–	–	–	–	–	–	–	–
SEL05	200	4.4	3	ns	–	–	–	–	–	–	–	–	–	–	–	–
SEL06	100	7.2	25/32		83 ± 4	21	0.57 ± 0.04	145 ± 11	11/12	176 ± 6	5.3 ± 2.2	1.41 ± 0.13	1.03 ± 0.03	166 ± 8	184 ± 8	145 ± 11
SEL07	100	7.2	24/35	close	100 ± 5	23	0.61 ± 0.04	163 ± 12	21/22	136 ± 5	4.5 ± 1.6	2.09 ± 0.13	1.07 ± 0.03	123 ± 6	144 ± 7	144 ± 7
SEL08	100	9.5	5	yes	67a		0.53 ± 0.04	126b	21/21	240 ± 3	4.4 ± 0.5	0.91 ± 0.18	0.99 ± 0.03	242 ± 9	259 ± 9	259 ± 9
SEL09	100	11.2	30/34		67 ± 3	20	0.57 ± 0.03	118 ± 9	19/21	123 ± 1	3.0 ± 0.2	1.4 ± 0.15	1.03 ± 0.03	117 ± 4	129 ± 5	118 ± 9

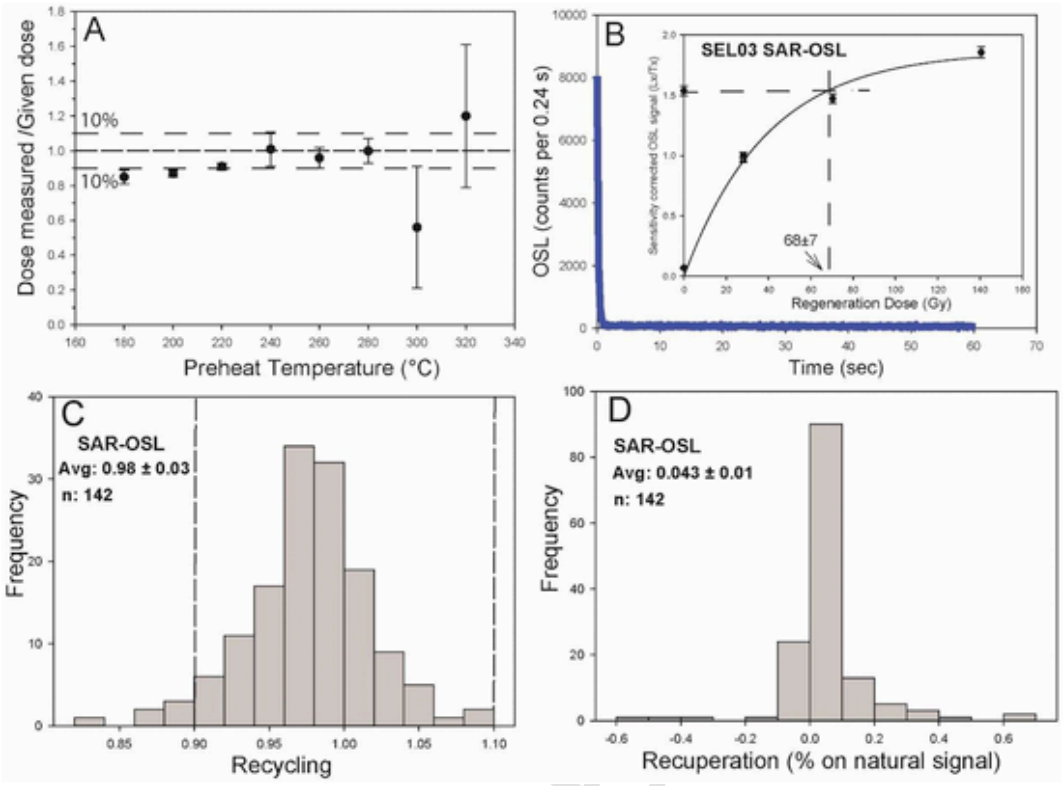

Fig. 5. A) Performance of dose recovery pre-heat plateau test of SAR-Protocol. **B)** Quartz OSL signal decay of the shinedown curve of sample SEL03. Signal decays in the first second of blue stimulation and thus it is dominated by fast component. Inset shows the saturation exponential fitted dose response curve (DRC) for sample SEL03. The OSL sensitivity corrected natural signal Lx/Tx is plotted on DRC and the equivalent dose is determined. **C)** Frequency distribution of recycling ratio obtained performing the SAR protocol set for this work; dashed lines highlight the rejection criteria values for aliquots. **D)** Frequency distribution of recuperation (% of signal after zero given dose on natural De) obtained performing the SAR protocol. (For interpretation of the references to color in this figure legend, the reader is referred to the Web version of this article.)

4. Results

4.1. Distribution and analysis of marine terraces

Both the elevation and the morphological characteristics of marine terraces changes in the three sectors of the study area (Fig. 3A and B). In the western sector, the elevation of the terraces inner margins steadily increases eastward from Capo Lilibeo to Capo Granitola. At the latter location, the trend of inner margins changes from NW-SE to E-W following the present coastline trend. The central sector extends from Capo Granitola to Capo S. Marco near Sciacca and includes the terrace maximum elevations (up to ~250 m). The western part of this sector between Capo Granitola and the mouth of the Belice River is referred to as the Selinunte Plain, and the eastern part from the Belice River to Capo S. Marco as the Menfi Plain. Finally, within the ~40 km long eastern sector that stretches from Capo S. Marco to Capo Bianco, the terraces show again a NW-SE trend and their elevation decreases in a manner anti-symmetrical respect to the western sector (Fig. 3B).

Like the inner margin elevations, also the width of terraces changes along the coastal plain. Moving from west to east, the average width of terraces increases from ~0.5 km in the western sector, to 1–2 km from Mazara area to the Belice River, and again narrows to ~0.5–1 km further east (Fig. 3A).

A thin (up to ~2–3 m) veneer of shallow-marine deposits, which generally consist of small to medium grained mixed carbonate-quartz sands, was observed above the wave-cut basal unconformity of the lower nine terraces (Table S1). The sand grains are composed of carbonate marine bioclasts (red algae, molluscs, echinoids, benthic foraminifera, and bryozoans) and variable amounts of quartz and feldspar. The sands are locally cemented to a degree that generally increases in higher and older deposits. Marine deposits are chiefly representative of a wave-dominated beach environment and include backshore, foreshore and shoreface facies associations deposited in a regressive barrier ridge system.

4.1.1. Terrace T1

The lowermost terrace, T1 has an inner margin between ~15 and 30 m elevation in the west and up to 33 m in few outcrops in the Selinunte Plain. The terrace is not mapped for 40 km between central and eastern sectors, where it briefly reappears at ~25 m (Fig. 3A and B). Deposits referred to T1 are exposed along the 2–3 m high coastal cliff by modern abrasion processes particularly in the western sector (logs #6, 7, 52, 65, 66, Table S1). The section logged at Torre Scibiliana (log #65; Fig. 4A) includes, above an abrasion platform carved in the Marsala Calcarenite and bored by *Lithophaga*, a rhodolith-rich calcarenite cemented by red calcareous (*Lithophyllum* spp.) algae (unit A; Fig. 7A–D). This unit is overlain by a bioclastic calcarenite with shelly layers (*Arca noae, Glycimeris glycimeris, Conus* cfr. *testudinarius*, *Bitta* spp., *Murex* spp., *Ostrea* spp., *Spondylus* spp.) and clumps of *Cladocora coespitosa* corals in life position (unit B; Fig. 7A, B, 7E, 7F). This upper calcarenite deposit includes 2-3 mm-thick laminar algal layers (Lm1 to Lm3, Fig. 7A) pointing to periodic oscillations of the sea-level. A specimen of *Persististrombus* cfr. *latus* was found not *in situ* above the described stratigraphic section (Fig. 7G). The fossil was highly fragmented and included in coarse clastic matrix, and this suggests reworking.

The Faro Granitola section exposed at the lighthouse near Capo Granitola (log #6; Fig. 4A; Table S1) has a basal unit that is not found at Torre Scibiliana. This basal unit (unit X, Fig. 8A–D) is composed of bi-directional cross-laminated quartz-carbonate sandstones (mixed siliciclastic carbonate deposits, *sensu* Chiarella et al., 2017). Unit X is followed by an algal calcarenite (unit A, Fig. 8E), by bioclastic sand-

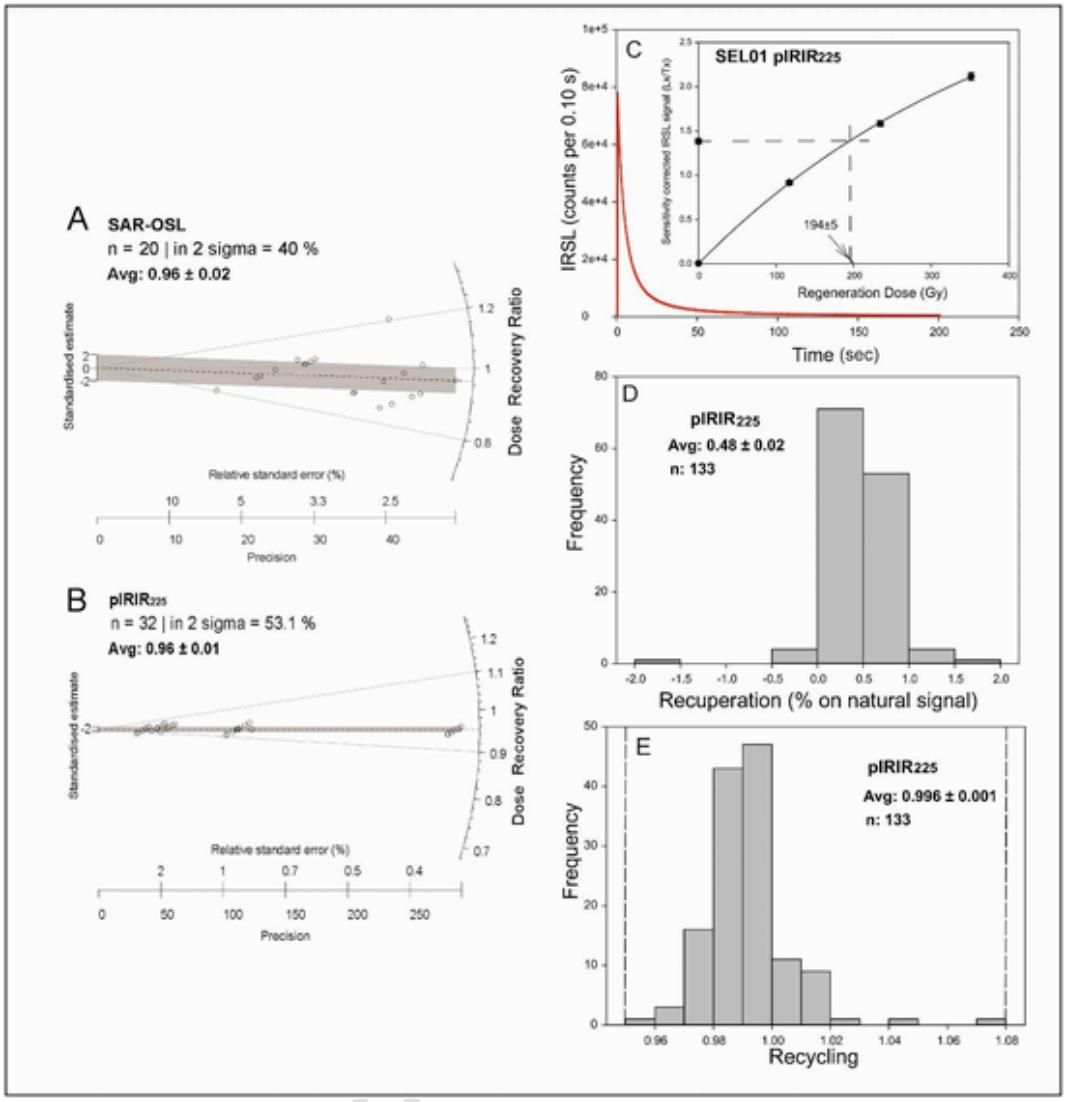

Fig. 6. - A) Radial plot of measured dose recovery ratio estimated for quartz samples using the SAR-OSL protocol. **B)** Radial plot of measured dose recovery ratio distribution and values of analyzed k-feldspar mineral measured with the pIRIR225 protocol. **C)** Typical pIRIR225 signal decay of shinedown curve of sample SEL01. Signal decays slower than OSL quartz signal. Inset shows the dose response curve (DRC) for sample SEL01. The IRSL sensitivity corrected natural signal Lx/Tx is plotted on saturation exponential fitted DRC and the equivalent dose is determined. **D)** Frequency distribution of recuperation (% of signal after zero given dose on natural De) obtained performing the pIRIR225. **E)** Frequency distribution of recycling ratio obtained performing the pIRIR225 protocol set for this work; dashed lines highlight the rejection criteria values for aliquots.

stones with shelly layers (unit B, Fig. 8F) and by calcretized sandstones with a basal conglomerate that contains bored clasts and blocks (unit C, Fig. 8G). Unit X and B are interpreted as being deposited in the upper shoreface and in the foreshore environment, respectively.

Based on the lithofacies association, we correlate units A to C exposed at Capo Granitola to units A-B at Torre Scibiliana. The section observed at Faro Granitola denotes higher environmental energy than the section found at Torre Scibiliana. Unit X instead is the oldest exposed unit considering both outcrops.

Well-sorted cuneiform, parallel-laminated and cross-laminated sandstones attributed to T1 are found in the Selinunte Plain (central sector) up to ~20 m and are referred to the fair-weather berm-backshore transition (**log #29,** Table S1; Fig. S1A**)**.

4.1.2. Terrace T2

The inner margin of T2 is traced quite continuously from ~30 to ~40 m in the western sector and more sparsely in the central sector between ~30 and 60 m. In the eastern sector, the inner margin descends from ~50 to 35 m elevation (Fig. 3A and B). Due to intense anthropic activity (particularly quarrying), the terrace is not easily visualized in the topographic profiles (Fig. 4B). No deposits referred to this terrace have been observed.

4.1.3. Terrace T3

The inner margin of this terrace is mapped in the west at elevations ranging from ~35 to ~55 m. In the central sector, the inner margin rises from ~55 to ~80 m, whereas in the east it descends from ~50 to ~25 m (Fig. 3B). Although the terrace is poorly preserved, its inner margin is well detected in the western sector (Fig. 4B, profile 3).

In the western sector, an abrasion platform carved in the Marsala Calcarenite between ~20 and 45 m elevation is associated to T3. The platform stretches for nearly 20 km from Mazara in the southeast to Marsala in the northwest and has a rather constant ~1 km width **(**Fig. 4A**)**. In addition, both maximum and minimum elevation of the platform decreases progressively to the northwest mirroring the pattern of its inner margin.

Locally, 1–2 m of regressive deposits attributed to T3 are found in both western and central sectors between ~40 and 50 m elevation, and consist of shoreface massive bioclastic sandstones (logs #32, 49, 71, Table S1; Fig. S1C). Within the incision of the Modione River in the

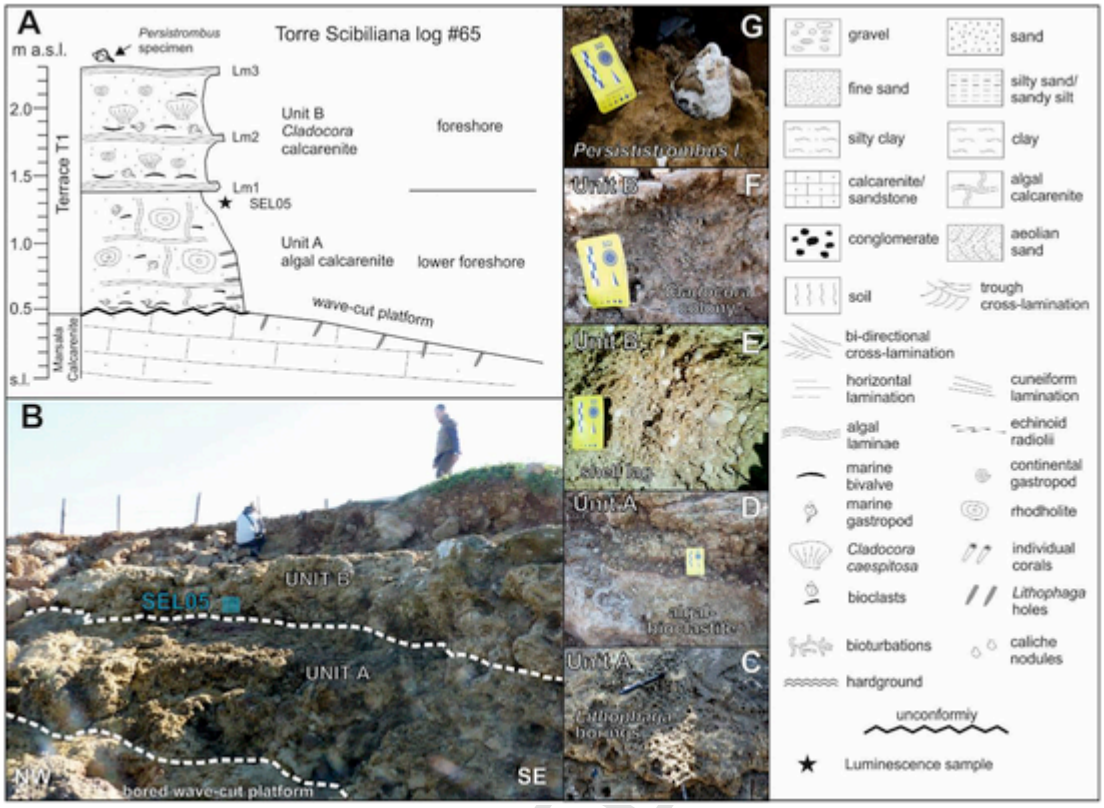

Fig. 7. Deposits of marine terrace T1 at Torre Scibiliana location (western sector): **A)** stratigraphic log; **B)** field stratigraphic relations, showing location of sample collected for luminescence dating; **C)** to **F)** details of units A and B; **G)** displaced specimen of *Persististrombus* cfr. *latus* found at the top of the outcrop. Here and in Fig. 6–10, the hashtag with number refers to the logs listed in Table S1 and located in Fig. 4A. Scale bar in D-E is 5 cm long and the pen in C is 12 cm long. On the right side of figure, general symbols key for stratigraphic logs in Fig. 7–10.

Selinunte Plain, 3 m of sands with basal fossil lags and calcarenites are found above the terrace at ~40 m elevation. The marine deposits pass upward to matrix supported fluvial conglomerates, plane laminated alluvial plain siltstones and high angle cross bedded aeolian sandstones (log #24; Table S1; Figs. S1B).

4.1.4. Terrace T4

The terrace has an inner margin whose elevation increases from ~50 to ~70 m in the west and from ~65 up to ~110 m in the central sector (Fig. 3B). After a 12 km gap, T4 is mapped again with fair continuity in the eastern sector where the margin smoothly descends from 75 to 55 m. The inner margin is readily identified in the Selinunte Plain, where the terrace is among the widest of the flight (Fig. 4B, profiles 2 and 3). In the west, T5 is associated with isolated remnants of an abrasion platform (Fig. 4A).

Several outcrops of deposits, whose thickness ranges between 1 and 6 m, are associated to this terrace at maximum elevations of between 60 and 70 m. In the western sector, they are represented by coarse bioclastic calcarenites with corals and mollusk shells, locally cemented by red algal concretions (logs #55, 58, 73, Table S1; Fig. S1D). In the central sector, at log #27 east of Campobello village (Fig. 4A), the upward transition from bi-directional cross-laminated coarse sandstones to plane-laminated coarse to medium sandstones is observed (Fig. 9A–C). These deposits are interpreted as the upper shoreface to foreshore parts of the barrier ridge system (Fig. 9A).

4.1.5. Terrace T5

The inner margin of T5 is mapped in the western sector at elevations increasing eastward from ~65 to ~100 m. After a ~10 m drop in the Selinunte Plain, elevation increases eastward from ~90 to ~135 m at the projection of M. Magaggiaro culmination. Only few remnants of T5 are mapped at ~125 m in the eastern sector and, at Capo Bianco at the termination of the study area, the terrace is found at ~80 m (Fig. 3B). The terrace is generally well identified in the Selinunte Plain (Fig. 4B, profile 2), less elsewhere. Few remnants of an abrasion platform are associated to this terrace near Marsala (Fig. 4A).

Deposits associated to T5 were only logged in the Selinunte Plain at up to ~75 m elevation and reach of thickness of 2.7 m (log #28, Table S1; Fig. 10A). Here, bioturbated fine sandstones form the lower unit A, and are covered by a paleosol (unit B). The overlying unit C is formed by locally channelized plane laminated sandstones, which are capped by high angle cross-bedded aeolian sandstones of unit D (Fig. 10A and B). Marine deposits of unit A are interpreted as being deposited in the lower shoreface, and those of unit C are assigned to the foreshore-backshore of a regressive barrier ridge. The occurrence of the paleosol between the two units and their inferred depositional environments suggest a minor sea-level oscillation. The aeolian sandstones of unit D are referred to dune order D4 that forms an evident ridge above this site (Fig. 4A).

4.1.6. Terrace T6

The terrace is traced continuously in the western sector, with an inner margin that increases in elevation from ~75 to ~125 m. The terrace elevation drops to ~110 m at Capo Granitola and increases again up to ~160 m south of M. Magaggiaro in the central sector. T6, as well as the overlying terraces were not observed in the eastern sector (Fig. 3A and B). North of Mazara (wester sector), T6 is characterized by remnants of an up to ~1 km wide abrasion platform (Fig. 4A).

Deposits of T6 are well exposed in the western part of the Selinunte Plain, where they reach up to ~110 m elevation and a thickness of ~2–2.5 m (logs #34, 36, 45, Table S1). At log #34, they are represented by bioturbated sandstones (unit A), overlain by trough-cross beds with

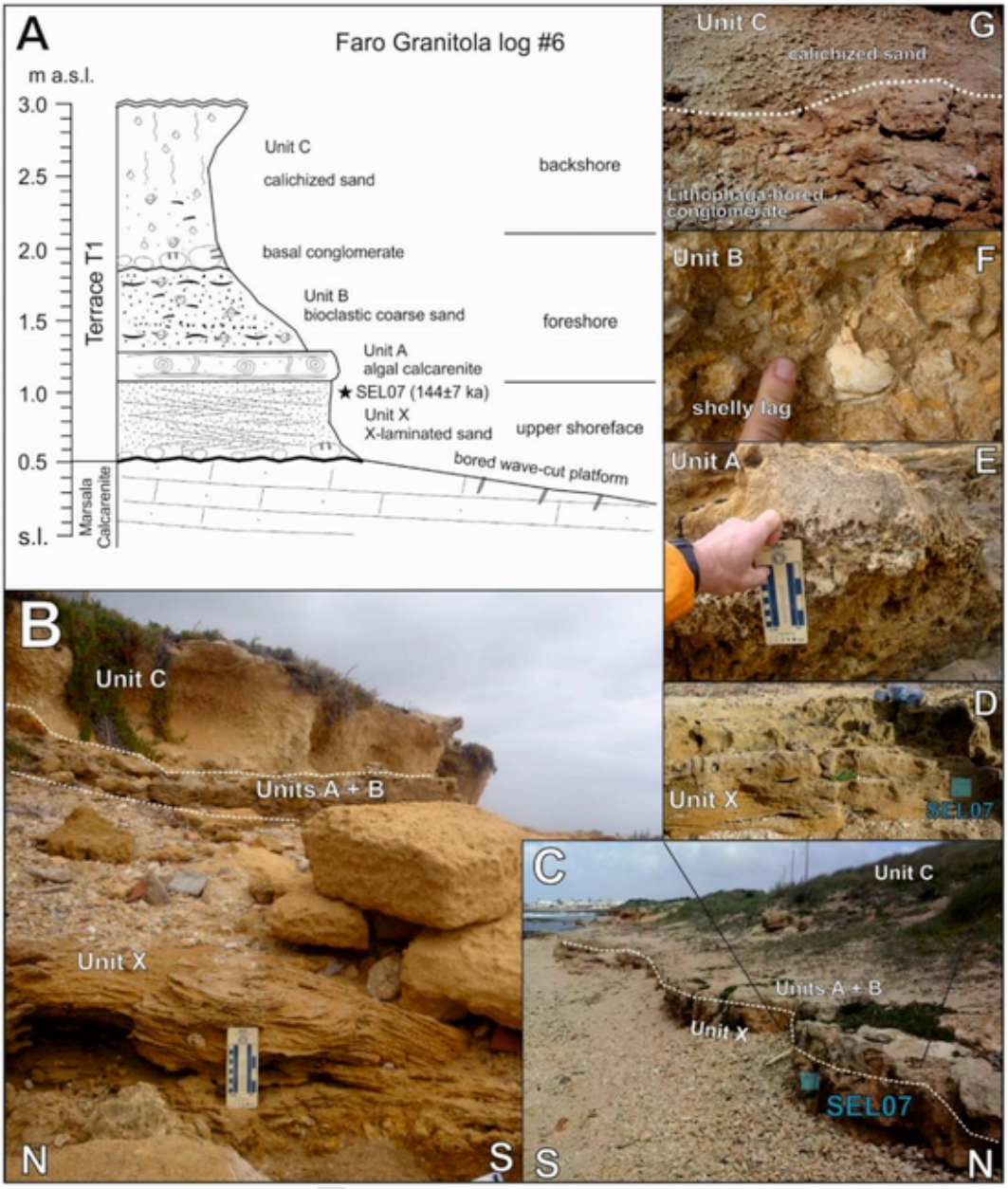

Fig. 8. Deposits of marine terrace T1 at Faro Granitola location (Selinunte Plain, central sector): **A)** stratigraphic log; **B)** and **C)** field stratigraphic relations, showing location of sample collected for Luminescence dating (also in inset D); **D)** to **G)** details of units A to D. Location in Fig. 4A.

bi-directional lamination sets (unit B) and plane laminated sandstones (unit C), which in turn grade into aeolian sands (unit D) (Fig. 10C and D; S2E). East of this location, fossiliferous pebble conglomerates followed by laminated bioclastic sandstones characterize a 2 m thick outcrop of T6 deposits, which sharply truncates above a ravinement surface deposits of an older terrace (log #100; Fig. S2A to S2C). In the western sector, 2 m of well sorted mixed bioclastic sands represents the terrace deposits (logs #59, 78; Table S1).

These deposits share similar characteristics in the different sectors, and are referred to the shoreface and foreshore parts of the barrier ridge system. The aeolian sandstones of unit D at log #34 represent the lower part of dune D5 that forms an evident ridge above this site (Fig. 4A).

4.1.7. Terrace T7

Few outcrops of T7 were mapped in the western sector, where the inner margin elevation rises from ~95 to ~140 m. In the central sector, the elevation increases from ~125 to ~170 m (Fig. 3B).

Scattered outcrops of marine deposits associated to T7 were observed in the Selinunte Plain (central sector). Here, at log #100 (Table S1), they are represented by 4 m of alternating fine and massive laminated sands that evolve to bioturbated sands (Fig. S2A to S2D). These deposits, which lie at ~115 m elevation can be correlated to 2 m of coarse bioclastic sands and conglomerates observed up to 125 m elevation at log #102; (Table S1). This lateral transition is interpreted as the passage from shoreface to foreshore deposits (Fig. S2E). The foreshore deposits outcrop further to the east in the Menfi Plain where they are represented by massive bioclastic sands (log #126, Table S1).

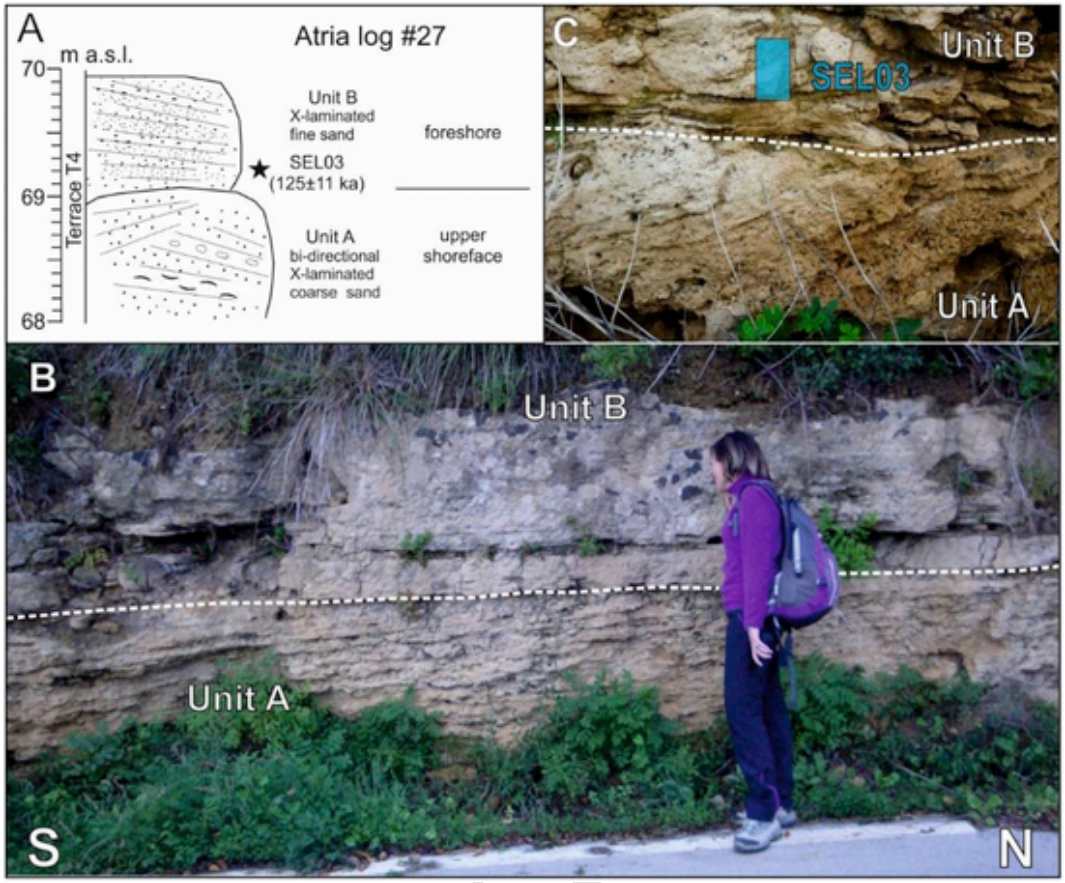

Fig. 9. Deposits of marine terrace T4 at Atria location (Selinunte Plain, central sector): **A)** stratigraphic log; **B)** field stratigraphic relations; **C)** detail of units A and B with location of sample collected for Luminescence dating. Location in Fig. 4A.

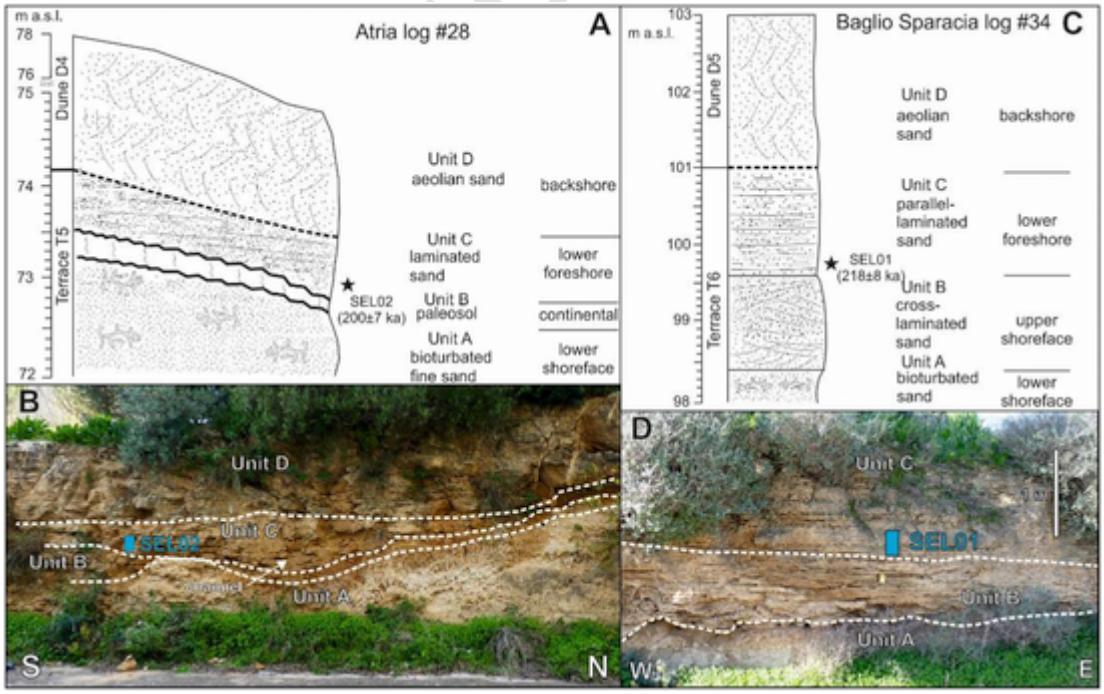

Fig. 10. Deposits of marine terraces T5 and T6: **A)** stratigraphic log and **B)** field stratigraphic relations of terrace T5 with location of sample collected for Luminescence analysis at Atria location (Selinunte Plain, central sector); **C)** stratigraphic log and **D)** field stratigraphic relations, with location of sample collected for Luminescence dating of terrace T6 at Baglio Sparacia location (Selinunte Plain, central sector). Location of both logs in Fig. 4A.

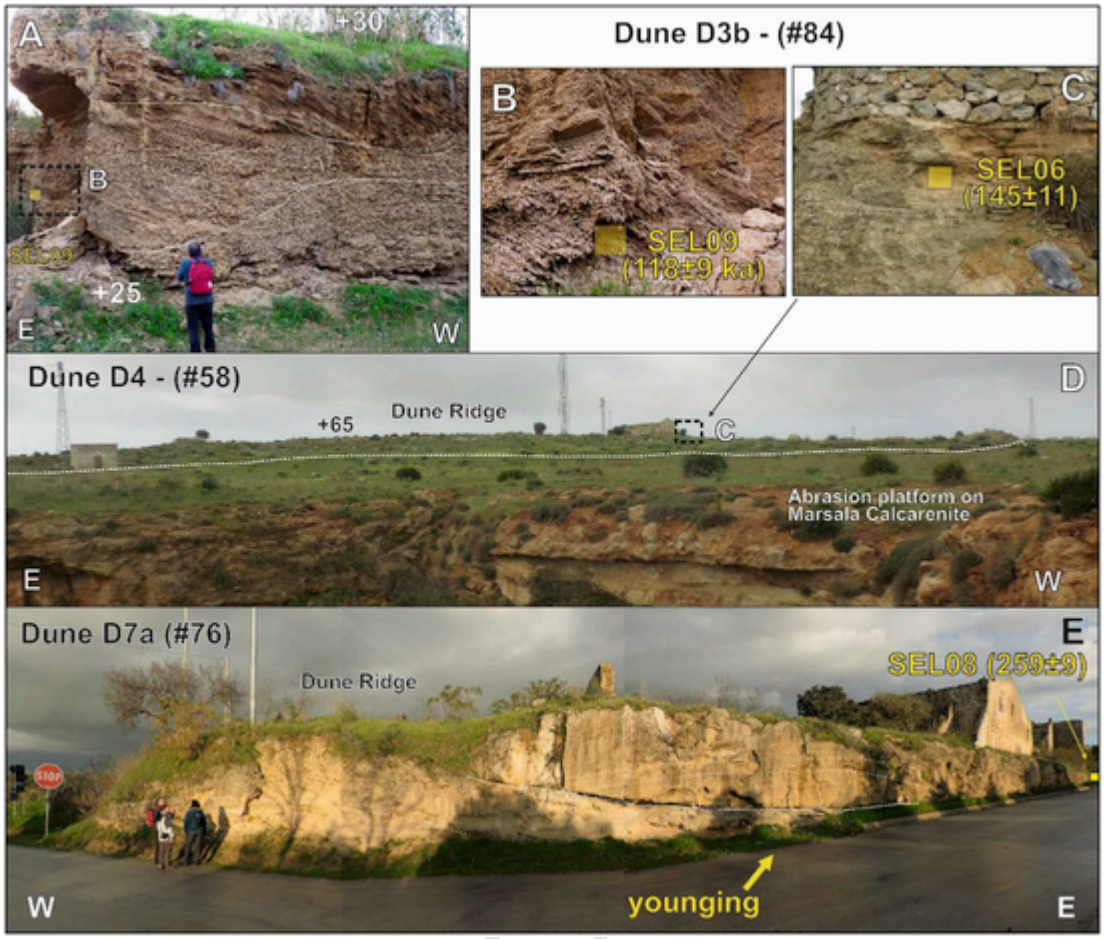

Fig. 11. Morphodepositional features of aeolian ridges: **A)** panoramic view and **B)** detail of dune D3b with location of sample collected for luminescence analysis at Timpani Nero location (Selinunte Plain, central sector); **C)** detail location of sample collected for OSL analysis from dune D4 at Timpone Maranzano (western sector); **D)** panoramic view of dune D4 at Timpone Maranzano; **E)** panoramic view of dune D8a with location of sample collected for luminescence dating at Case Pardo (western sector). Location in Fig. 4A.

4.1.8. Terrace T8

The inner margin of T8 ranges from ~105 to 145 m in the west and from ~150 to 210 m in the central sector (Fig. 3B). Sparse deposits are found on this terrace north of Mazara village (western sector) between ~130 and 150 m elevation and are represented by loose fossiliferous calcarenites and locally well cemented pebble conglomerates (logs #70, 76 and 119, Table S1; Fig. S3A, S3B). These deposits have been interpreted as upper shoreface and beachface deposits, respectively, of a barrier ridge system.

4.1.9. Terraces T9 to T11

Remnants of the higher terraces are preserved unevenly in the central sector only (Fig. 4A). The inner margin elevation of T9 increases between ~175 and 250 m from the Selinunte Plain to the M. Magaggiaro culmination. Conversely, the inner margin of the highest terraces is only mapped at ~190–220 m (T10), at ~240 m (T11) in the Selinunte Plain and not in the sector of maximum uplift (Fig. 3A and B).

Deposits associated to these higher terraces were only observed on T9 north of Mazara village (central sector). Here (log #62, Table S1), high angle, bioturbated cross-bedded sandstones and nodular bioclastic calcarenites resting on a basal paleosol, are developed on different Pleistocene and Pliocene units (Fig. S3C to S3E). These deposits have been interpreted as lower foreshore and upper shoreface deposits.

4.2. Distribution and analysis of aeolian ridges

One of the most prominent features of the southwestern Sicily coast is represented by narrow and long ridges standing above the surrounding landscape. They are readily identified both in map view (Fig. 4A) and in profiles, where they are evidenced by peaks in the slope % value (Fig. 4B). Ridges have lengths up to ~10 km (Fig. 4A), and height and width of tens and hundred meters (Fig. 4B), respectively. Generally, height and width increases with elevation of ridges. Their trend progressively changes to keep sub-parallel to the present coastline and to the inner margins of terraces (Fig. 4A).

As outlined before, geomorphology, facies analysis and stratigraphic relationships with the underlying marine deposits document that the ridges represent former coastal dunes (e. g. Andreucci et al., 2010; Sloss et al., 2012). Individual ridges are composed of single dune bodies or, more commonly, by several prograding and aggrading bodies often separated by erosive surfaces (Fig. 11A and E). The dunes consist of planar or trough cross-bedded, well sorted, medium to coarse-grained pale brown sandstones (Fig. 11A, B, 11E). They are moderately to well cemented; cementation degree increases landward, suggesting a concurrent increasing age of the ridges. The sand grains mostly consist of reworked marine carbonate bioclasts with subordinate occurrence of quartz and feldspar. Occasionally, terrestrial gastropods and rhizoliths, some of which are moulds and others are calcified root casts, occur. At several locations, these cross-bedded deposits overlie with a gradual transition the underlying beach deposits (Fig. 10A–C).

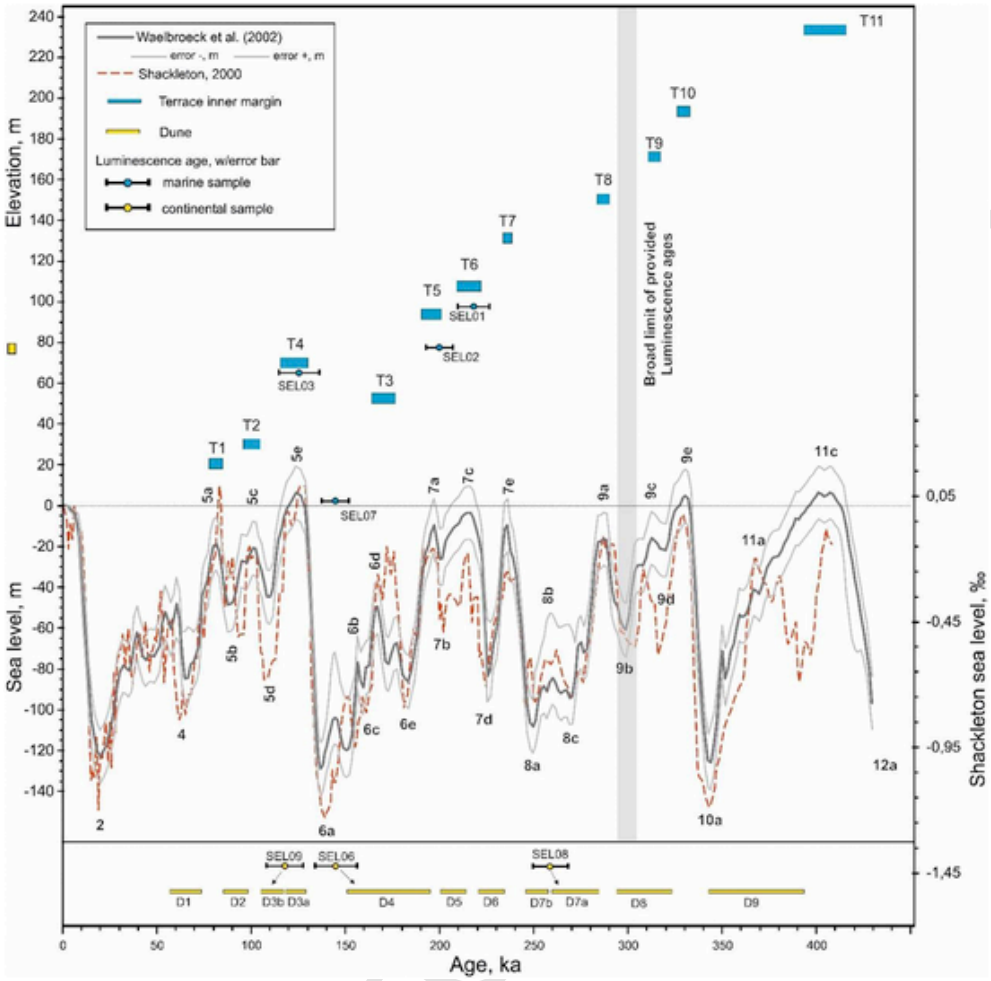

Fig. 12. – Luminescence age results and dating of marine terraces and dunes. Global sea-level curves from Waelbroeck et al. (2002) and Shackleton (2000); MIS nomenclature from Railsback et al. (2015). Elevation of inner margin of marine terraces refers to the Selinunte Plain transect (Fig. 3B); the horizontal bar for each terrace data point is proportional to estimated sea-level stand duration, the vertical bar is the estimated positioning uncertainty. Luminescence ages (1σ errors, Bateman et al., 2015) of marine deposits are plotted at the sample elevation beneath the related terrace. Estimated ages of aeolian dunes along with luminescence ages for dunes D3b, D4 and D7a are shown below the sea-level curves.

Locally, the contact is marked by caliche or by carbonate concretions. Observed paleo-wind directions are mostly aligned from NW-SE to NE-SW.

In addition to the modern and recent loose dunes, we mapped nine orders of dune ridges (D1-D9) between ~10 and 230 m of elevation (Fig. 4A and B). The ridges are best preserved in the Selinunte Plain, more scattered in the western sector, and almost missing east of the Belice River, where the coastal plain is narrower. Dunes D3 and D7 are further subdivided in two sub-orders (D3a, D3b and D7a, D7b).

As a first step, we correlated the dune ridges based on their lateral continuity, size and the elevation of the ridge toe. We choose the toe and not the top because tops of aeolian ridges display uneven natural elevations and are more subject to erosion. The major change in trend of the dune ridges occurs at the transition between western and eastern sectors (Fig. 4A).

4.3. Luminescence chronology

We collected six samples from marine deposits of terraces T1, T4, T5, T6, and three samples of aeolian sands from dune ridges D3b, D4 and D8a (Tables 1–4). The luminescence chronology was established using both quartz SAR-OSL and $pIRIR_{225}$ dating luminescence protocols. Reliability of ages were based on laboratory tests and depositional characteristics and stratigraphic relationship. Calculated ages with additional information are summarized in Table 2. With no specific age model being applied, all luminescence ages are derived from mean equivalent doses after rejection criteria application, divided by the dose rate determined for the specific sample. Quartz samples SEL01, SEL02 and SEL08 showed the natural sensitivity OSL signal beyond the saturation limit of reliability and, therefore only minimum ages were calculated (Table 2). Quartz Samples SEL04 and SEL05 from terrace T1 show OSL signal characteristics that do not allow age calculation. Quartz sample SEL07 gave an OSL-age of about 163 ± 12 ka but it shows a natural sensitivity OSL signal very close to the saturation limit, thus, the derived age may be over or underestimated (Wintle and Murray, 2006). The remaining quartz samples SEL03, SEL06 and SEL09 gave reliable SAR-OSL ages of 125 ± 11 ka, 145 ± 11 ka and 118 ± 9 ka respectively.

The $pIRIR_{225}$ dating protocol on K-feldspar grains was applied on all samples except for SEL03, SEL04 and SEL05 because no suitable material was obtained after the laboratory treatments. The $pIRIR_{225}$ fading-corrected derived ages are 218 ± 8 ka (SEL01), 200 ± 7 ka (SEL02), 184 ± 8 ka (SEL06), 144 ± 7 ka (SEL07), 259 ± 9 ka (SEL08) and 129 ± 5 ka (SEL09).

To define the most precise chronological framework for the studied paleoshorelines, either quartz or K-feldspar derived ages were selected based on the following criteria:

Table 3
– Luminescence age, MIS attribution, and estimation of the uplift amount and rate for marine samples. The luminescence ages are either from quartz SAR-OSL (#) or feldspar pIRIR225 (^) analysis (Table 2). The uplift has been computed by adding to the present sample elevation the estimate of the global sea-level position at the related MIS highstand (from Waelbroeck et al., 2002).

Sample code	Coordinates	Sample elevation (m)	Luminescence Age (ka)	MIS	Global sea level (m)	Uplift (m)	Uplift rate (mm/a)	Average uplift rate
SEL01	37°38′39.79″N 12°47′16.80″E	99.5 ± 2	218 ± 8^	7c	−4±13	104 ± 15	0.48 ± 0.07	0.48 ± 0.14
SEL02	37°37′48.70″N 12°47′38.68″E	73 ± 2	200 ± 7^	7a	−10 ± 13	83 ± 15	0.42 ± 0.08	
SEL03	37°37′35.00″N 12°47′40.02″E	65 ± 2	125 ± 11 #	5e	6 ± 13	61 ± 15	0.49 ± 0.12	

Table 4
- Luminescence age results, MIS attribution and estimation of the elevation above the coeval sea-level for aeolian samples. The luminescence ages are either from quartz SAR-OSL (#) or feldspar pIRIR225 (^) analysis (Table 2). Global sea-level position from Waelbroeck et al. (2002). The uplift has been computed using the luminescence age and an average uplift rate of 0.5 mm/a (see Table 3). The paleo-elevation has been estimated combining present elevation, computed uplift and estimated lowermost sea level during correlative MIS based on Waelbroeck et al. (2002).

Sample code	Location	Coordinates	Elevation (m a.s.l.)	Dune order	Luminescence age (ka)	MIS	Global sea level (m)	Uplift (m)	Paleo-elevation (m)
SEL08	C.se Pardo	37°40′13.38″N 12°45′38.17″E	152 ± 2	D7a	259 ± 9^	8a-8c	−85 ± 13	130 ± 15	107 ± 15
SEL06	Timpone Maranzano	37°40′40.62″N 12°36′35.39″E	65 ± 2	D4	145 ± 11 #	6b-6a	−104 ± 13	73 ± 15	96 ± 15
SEL09	C.se Ferracano	37°35′36.71″N 12°46′37.18″E	27 ± 2	D3b	118 ± 9 #	5d	−45 ± 13	55 ± 15	13 ± 15

1) natural OSL signal is zeroed under the sun-light faster than the pIRIRSL signal, thus quartz derived ages are selected if the signal is not close or fully saturated because less prone to partial-bleaching phenomenon compared to the pIRIRSL;
2) if the natural quartz OSL signal is close to saturation the K-feldspar derived age is selected because quartz OSL-derived ages may over or underestimate the "*true*" age (e.g. Wintle and Murray, 2006; Buylaert et al., 2012);
3) if the natural quartz OSL signal is fully saturated the K-feldspar derived age is selected because its range usually extends beyond the limits of quartz-derived ages (e.g. Buylaert et al., 2012; Andreucci et al., 2014; 2017; Pascucci et al., 2014; Sechi et al., 2020).

Based on the above criteria seven over nine samples are considered appropriate to build a chronological framework of the studied deposits. Four of them are from marine (SEL01; SEL02; SEL03; SEL07) and the remaining three (SEL06, SEL08, SEL09) from aeolian deposits.

4.3.1. Marine deposits

The preferred luminescence ages allowed assigning the dated deposits and the related terraces to highstands and interstadial stillstands of the Middle-Late Pleistocene. The lowermost dated sample (SEL07) from the basal unit X exposed at the Faro Granitola site yielded a luminescence final age of 144 ± 7 ka (Fig. 8A; Table 2) indicating that the sands were deposited during MIS 6b (Table 3).

Samples SEL01, SEL02 and SEL03 come from the terrace staircase of the Selinunte Plain (Figs. 3B and 4A) and yielded stratigraphically ordered results. Sample SEL03 comes from the base of the foreshore sandstones of terrace T4 and yielded an age of 125 ± 11 ka (Fig. 9A; Table 2). Thus, T4 is assigned to the last interglacial, MIS 5e (Table 3). Sample SEL02 from the base of the foreshore sandstones (unit B) of T5 yielded an age of 200 ± 7 ka (Fig. 10A; Table 2), allowing to assign this terrace to MIS 7a (Table 3). Finally, sample SEL01 from the foreshore sandstones of T6 yielded a final age of 218 ± 7 ka (Fig. 10C; Table 2), and constrained the age of this terrace to MIS 7c (Table 3).

4.3.2. Aeolian deposits

Sample SEL09 from dune ridge D3b in the Selinunte Plain (Fig. 4A) provided a final age of 118 ± 9 ka (Fig. 11A and B; Table 2), documenting that these dunes formed soon after the last interglacial highstand, and specifically during substage 5d (Table 4). Sample SEL06 from dune ridge D4 north of Mazara (Fig. 4A) yielded a final age of 145 ± 11 ka (Figs. 10C, D; Table 2), and thus was deposited in the last part of MIS 6 (Table 4). The sample was collected from the upper part of the dune (Fig. 11C and D), suggesting that dunes D4 span the MIS 6.

Finally, sample SEL08 comes from dune ridge D7a west of Castelvetrano (Fig. 4A). This composite dune system is one of the largest in the study area and includes several aeolian bodies. The sample was collected in one of the highest and youngest body of the ridge and provided a final age of 259 ± 9 ka (Fig. 11E; Table 2). This age documents that the dunes formed during MIS 8 (Table 4).

5. Interpretation

5.1. Correlation of terraces with sea level highstands

The existence of a staircase of marine terraces attests that coastal uplift has occurred in southwestern Sicily and that the age of terraces should increase with their elevation. By combining mapping, sedimentological analysis and luminescence dating results for same of the terraces, it is possible to suggest a correlation with MISs for all the terraces of the staircase (Fig. 12).

Specifically, we use the uplift rate computed from the position of dated samples to match the observed elevation of undated terraces and the elevation predicted for highstand shorelines of the sea-level curve (following the nomenclature of Railsback et al., 2015). We compute the sample uplift by adding to their present elevation the paleo sea-level position of related highstands from the curve of Waelbroeck et al. (2002). We have selected this curve, because a large number of

coastal studies have referred to it (e. g., de Gelder et al., 2020, and references therein).

The adopted uplift uncertainty combines the uncertainty in estimations of global sea-level (±13 m during the last ~250 ka according to Waelbroeck et al., 2002) and the error in field positioning (±2 m, see Method section). We do not include the uncertainty deriving from luminescence ages to avoid unrealistic estimates of paleo sea-levels. Results indicate that dated samples have been uplifted on average at a rate of 0.48 ± 0.14 mm/a (Table 3).

Because three (SEL01, SEL02, SEL03) out of four dated marine samples come from the Selinunte Plain and are distributed along a single transect when projected on the coast-parallel profile of terraces inner margin, we infer the age of undated terraces along the Selinunte Plain transect (Fig. 3B; Table 5). To this end, we extract the inner margin elevation of all terraces along the transect to evaluate the deviation of this elevation with respect to the predicted position of Middle-Late Pleistocene highstands using the computed average uplift rate of 0.5 mm/a as a constraint. In addition to dated marine samples, we use the luminescence age of aeolian dunes to place an upper age limit on the underlying terrace.

We estimate that terraces T1 to T11 have Middle-Late Pleistocene ages ranging between ~80 and 400 ka (Table 5; Fig. 12). In detail, terraces T1 and T2 are assigned to MIS 5a (~80 ka) and 5c (~100 ka), respectively. The 118 ± 9 ka (MIS 5d) age of dune D3b, which rests above T2, supports the attribution of this terrace to MIS 5c (Figs. 4A and 12).

The luminescence age of sample SEL07 (144 ± 7 ka), which comes from the upper shoreface sandstones (unit X) at the base of the sedimentary section exposed at Faro Granitola, creates an apparent conflict with the MIS 5a age (~80 ka) assigned to terrace T1 based on the extrapolated uplift rates. The age of SEL07, although correct from both a luminescence and a stratigraphic perspective, complicates the otherwise consistent chronological scheme and the estimated uplift history of the area and, therefore, it is not considered realistic.

Using an uplift rate of 0.5 mm/a, we refer terrace T3 to MIS 6d (~165 ka), the major interstadial occurring during the sea-level fall that followed MIS 7. In support of the age attribution, we recall that T3 is surmounted by dune D4, whose upper part has been dated at 145 ± 11 ka (MIS 6b-6a; Fig. 11C and D; Table 4).

Luminescence age of sample SEL03 document that terrace T4 formed during MIS 5e (~125 ka). Terraces T5 and T6 have deposits with luminescence ages that document their formation during MIS 7a (~200 ka) and 7c (~215 ka), respectively (Fig. 12). Overlying terraces T7 and T8 are assigned to MIS 7e (~240 ka) and MIS 9a (~290 ka), respectively. The age attribution for these two terraces based on the uplift rate determined from samples coming from lower terraces is supported by the luminescence age result (259 ± 9ka, MIS 8) for the upper part of dune D7a, which, together with dune D7b, is interposed between the two terraces (Fig. 4A; Fig. 12).

No direct or indirect luminescence age constraints are available for higher and older terraces. Using the uplift rates from lower terraces, T9, T10 and T11 are assigned to MIS 9c (~310 ka), MIS 9e (~330 ka) and MIS 11c (~400 ka) highstands, respectively (Table 5; Fig. 12).

5.2. Model of aeolian dunes formation

Luminescence age results from aeolian dunes indicate that they formed during both major and minor lowstands of the global sea-level curve (Fig. 12; Table 4). With sea-levels lower than the present and a gentle shelf bathymetry, large amounts of sands were available to wind transport inland from the shelf. This process was enhanced by dry and cold climatic conditions that favored the reworking of marine sediments and the growth of aeolian bodies as documented at several Mediterranean coasts (Nielsen et al., 2004; Fornos et al., 2009; Andreucci et al., 2010, 2017; Thiel et al., 2010; Pascucci et al., 2014, 2019; Elshazy et al., 2019; Casini et al., 2020; Sechi et al., 2020).

The intimate spatial relation between terrace inner margins and dunes, locally supported by luminescence ages, supports the contention (e. g., Andreucci et al., 2010; Sechi et al., 2020) that lowstand dune bodies formed above the previous highstand terrace. More in detail, the locally observed gradational transition between beach deposits and overlying aeolian deposits (Fig. 10A–D) indicate that dunes mostly formed during the regression following interglacial stages.

Bearing the above in mind, we argue that each terrace and overlying dunes located at its inner margin or seaward of it are part of the same transgressive-regressive cycle. Fig. 13 is a schematic representation of this evolutionary model. During an interglacial period, a marine terrace forms and hosts a thin shallow-water deposit likely because of the relatively limited sediment supply at this coast (Tn, Fig. 13A). During the ensuing relative sea-level fall, aeolian sediments buttress against the slope above the terrace inner margin and a dune ridge develops above and often continuously with the marine deposits (riser dune; Fig. 13B). Some dunes, usually of lesser size, continue developing seaward of this position as the sea level progressively drops, possibly by growing upon pre-existing bathymetric features such as submarine bars (terrace dune; Fig. 13B). The process regularly repeats during younger transgressive-regressive cycles (Fig. 13C).

Although simplistic, the model satisfactorily reproduces the observed sub-parallelism between terraces inner margins and dunes and predicts that in an uplifting coast, terraces and dunes belonging to individual transgressive-regressive cycles are sequentially preserved and not randomly distributed. Using the luminescence constraints on aeolian deposits and the model of dune formation, we infer that the ages of the nine dune orders spans between ~60 ka (MIS 4) and ~400 ka (MIS 11) (Fig. 12; Table 6).

Dunes D1 and D2, which are developed to a lesser extent than overlying dunes (Fig. 4A), are attributed to minor lowstands (MIS 4 and 5b) of the last sea-level fall. Dunes D3a and D3b appear better developed instead and represent in our reconstruction the riser and terrace dunes, respectively, which grew following the last interglacial. The attribution of D3b to MIS 5d is constrained by the luminescence age of sample SEL09 (Fig. 12). We checked the reliability of our model by computing the elevation of D3b above the coeval sea level using its present elevation, the amount of its uplift, and the eustatic sea-level position at the time it formed. Results agree with the model and only impose to adjust the nominal age of sample SEL09 in Figs. 12 to 110 ka (within the luminescence age uncertainty, 118 ± 9 ka) to avoid an estimation that would locate the dune beneath the coeval sea-level. On this basis, and because sample SEL09 comes from near the base of the dune (Fig. 11A and B), we infer that D3b started forming 15 m above sea level during MIS 5d in a backshore position and then evolved within a coastal plain as sea level progressively dropped (Table 4). The ensuing transgression related to the MIS 5c rise flooded the coast just below this aeolian ridge, which was thus preserved (see Fig. 13C). The more inward dune D3a is developed onto the riser of the last interglacial terrace, and thus it has a 5e-5c assigned age.

Dunes D4 are mostly developed inward of T4 and thus are older than the last interglacial. A dune of this order is preserved near Mazara above the inner margin of terrace T3 (Fig. 4A), and is related to MIS 6 by the luminescence age of sample SEL06 that was collected from the top of the aeolian succession (Fig. 11C and D). The position of the sample suggests that the dune may have started growing onto the riser of T3 some (ten?) thousand years before, at the end of MIS 6d, and became a relict dune when sea-level dropped to a point that the dune was no longer connected to the coastal sector. Based on this, the dune is attributed to MIS 6, with its top having an age likely constrained by the maximum age of SEL06 (Table 4; Fig. 12). Dunes D4 in the Selinunte Plain have grown gradually above deposits of terrace T5 attributed to MIS 7a (Fig. 10A and B), further supporting the contention that this

Table 5
– Chronology of marine terraces based on correlation with Marine Isotopic Stages, and estimation of the average and time-partitioned uplift rate in the Selinunte Plain and M. Magaggiaro transects. Global sea-level highstands age and depth relative to present from Waelbroeck et al. (2002). The last four columns are valid for both transects and list: the terrace couplets used to calculate the time-partitioned uplift rate; the average uplift uncertainty, deriving from errors in positioning and uncertainty in global sea-level estimation; the related average and time-partitioned uplift rate uncertainty.

Marine Isotopic Stage			Terrace order	Selinunte transect				Magaggiaro transect				Magaggiaro & Selinunte transects			
Stage	Age (ka)	Paleo sea level (m)		Inner margin eevation (m a.s.l.)	Average uplift (m)	Average uplift rate (mm/a)	Incremental uplift rate (mm/a)	Inner margin eevation (m a.s.l.)	Average uplift (m)	Average uplift rate (mm/a)	Incremental uplift rate (mm/a)	Terrace couplets	Average uplift uncertainty (m)	Average uplift rate uncertainty (mm/a)	Incremental uplift rate uncertainty (mm/a)
11c	406	6	T11	234	228	0.56	0.53					T11/T10	±18	±0.04	±0.24
9e	331	5	T10	193	188	0.57	0.33					T10/T9	±18	±0.05	±1.00
9c	313	−16	T9	166	182	0.58	0.57	241	257	0.82	1.19	T9/T8	±18	±0.06	±0.69
9a	287	−16	T8	151	167	0.58	0.76	210	226	0.79	0.90	T8/T7	±18	±0.06	±0.35
7e	236	−9	T7	132	128	0.54	0.76	171	180	0.76	0.90	T7/T6	±18	±0.08	±0.86
7c	215	−4	T6	108	112	0.52	0.33	157	161	0.75	0.83	T6/T5	±18	±0.08	±1.00
7a	197	−10	T5	96	106	0.54	0.20	136	146	0.74	0.53	T5/T3	±18	±0.09	±0.60
5e	124	6	T4	70	64	0.51	0.62	110	104	0.84	1.19	T4/T2	±18	±0.14	±0.86
6d	167	−50	T3	50	100	0.60	0.84	80	130	0.78	0.60	T3/T4	±18	±0.11	±0.42
5c	103	−21	T2	30	51	0.50	0.62	58	79	0.77	1.29	T2/T1	±18	±0.17	±0.86
5a	82	−19	T1	19	38	0.46		33	52	0.63			±18	±0.22	

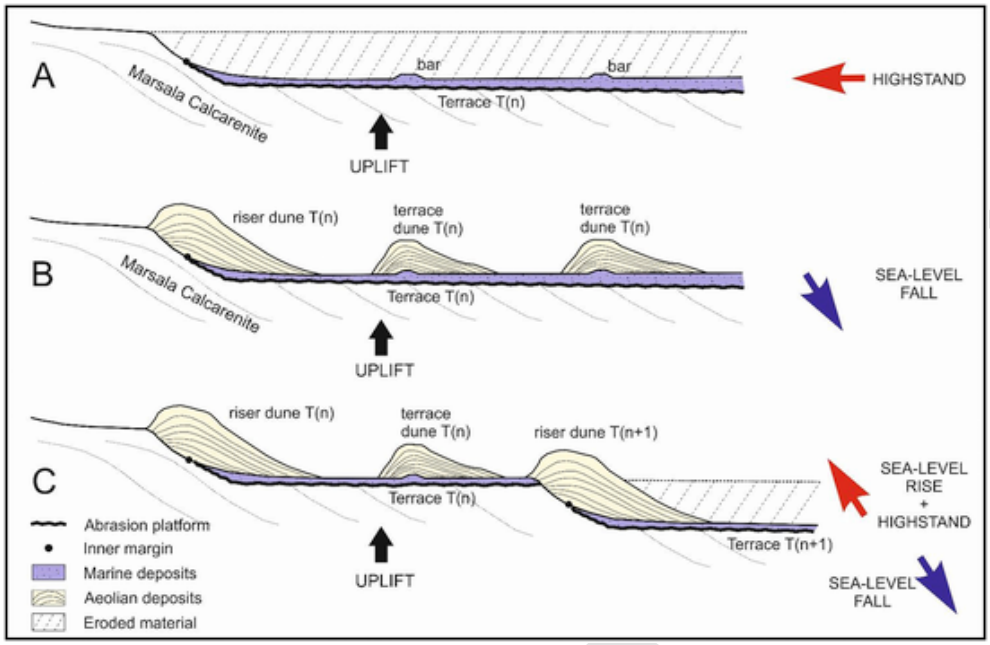

Fig. 13. Sketch showing formation of a coastal dune above the inner margin or the surface of a previous marine terrace during land uplift and eustatic sea-level cycles. See text for explanation of the illustration.

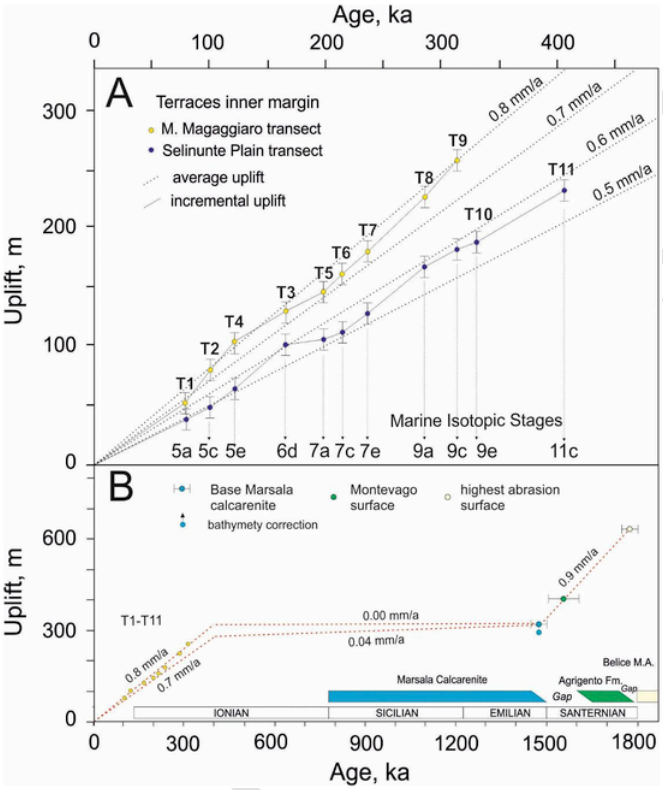

Fig. 14. Uplift history for southwestern Sicily: **A)** Middle-Late Pleistocene average and incremental uplift against age along the M. Magaggiaro and Selinunte transects for marine terraces T1 to T11 during the last ~400 ka; **B)** Pleistocene average uplift against age approximately spanning the area of maximum uplift rate (M. Magaggiaro transect). See text for details.

order developed during the regression following the penultimate interglacial (Fig. 12).

Similarly, dunes D5 in the Selinunte Plain are found inward of T5 and have grown gradually above marine deposits of T6 attributed to MIS 7c (10C, 10D), indicating that they formed during the regression leading to stillstand 7b (Fig. 12). Although stratigraphic relation with underlying marine deposits are not observed for dunes D6, they are found just sea-ward of the inner margin of T7 (MIS 7e) and are thus related to MIS 7d (Fig. 4A).

The wider-developed dunes D7a and D7b are interpreted as riser and terrace dunes, respectively, formed above terrace T8 (MIS 9a). The interpretation is supported by the luminescence age of sample SEL08 from dune D7a, which constrains within uncertainty the attribution of this dune system to MIS 8c. We estimate that D7a, one of the largest of the area and composed of several generations of dunes (Figs. 4a and 11E) started forming in the backshore of T8 and continued growing when the sea-level progressively fell. This estimation is supported by position and age of sample SEL08 that was collected from the upper part of the aeolian section and returned a lowstand-peak age, with an estimated elevation of ~100 m above the coeval sea-level (Table 4; Figs. 11E and 12).

Direct or indirect age constraints are not available for higher dune orders, but their position relative to terrace inner margins (Fig. 4A), and extrapolation of observations and interpretations for lower dunes indicate a similar age relation with terraces (Table 6). Specifically, D8 is developed above the riser of terrace T9 (MIS 9c) and is thus assigned to MIS 9b-9d. Similarly, D9 develops on T11 riser (MIS 11c) and we refer it to MIS 11a-10a (Fig. 12).

6. Discussion

6.1. Timing and rates of Middle-Late Pleistocene uplift

As illustrated above, the direct and indirect dating of raised marine terraces demonstrates that southwestern Sicily has experienced tectonic uplift at a significant pace. Although previous coastal studies did document that uplift has occurred in this region, contrasting views exist regarding the timing and amount of displacement.

Based on the previously reported findings of *Persististrombus* specimens at elevations near present sea-level at Torre Scibiliana and Mazara del Vallo sites in the western sector (Ruggieri and Unti, 1974), D'Angelo and Vernuccio (1996) argued that their lowermost terrace (corresponding to our T1) formed during MIS 5e. Their conclusion together with the observation that seven additional terraces in-

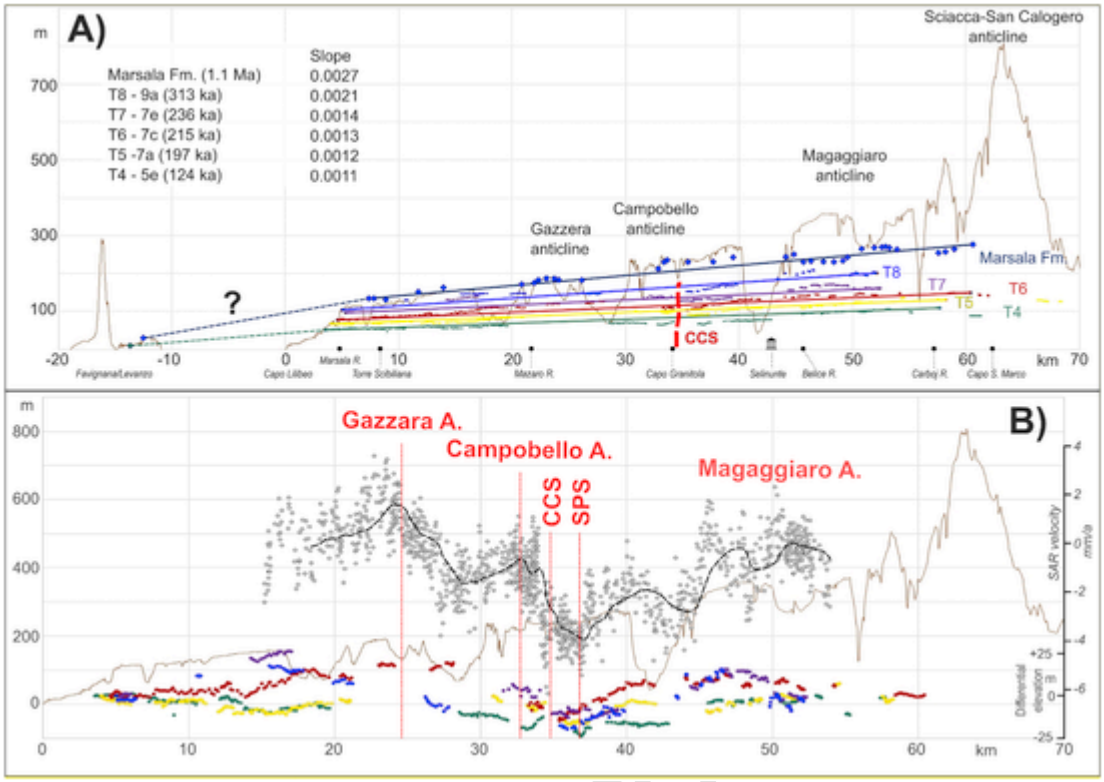

Fig. 15. – A) Inner margins elevations of terraces T4 to T8 and maximum elevation of Marsala Calcarenite innermost outcrops projected onto a N135 striking profile (see Fig. 3B), with linear regressions showing a southeastward increase of overall uplift scaled with terrace age. Assigned average ages in parenthesis. This southeastward increase in uplift highlights the regional tectonic signal. The elevation of the MIS 5e terrace (Ferranti et al., 2006; Antonioli et al., 2018) and of the Marsala Calcarenite (from official geological maps: https://www.isprambiente.gov.it/Media/carg/sicilia.html) in the Favignana and Levanzo islands to the northwest is also reported. **B)** Profile of the Line Of Sight (LOS) mean velocity data obtained from Interferometric Synthetic Aperture Radar (InSAR) observations (redrawn from Barreca et al., 2014). The InSAR profile is roughly parallel (see Fig. 2A for the trace) to the terrace displacement profile (top). Differential elevation profile between mapped and expected elevation of the inner margins of terraces T4 to T8, highlighting local tectonic signals with a wavelength of ~10 km (bottom). A spatial correspondence between peaks and lows of InSAR and differential elevation of terraces is apparent. The peaks correspond to the Gazzara, Campobello and Magaggiaro anticlines, and the low to the Selinunte Plain Syncline (SPS) (see Fig. 2A and B for location of tectonic structures). A drop in interferometry and terrace data occurs across the Castelvetrano-Campobello Scarp (CCS). In both Fig. 15A and B, the solid line is the topographic profile (trace in Fig. 3A).

cluding the GTS lay above the lowermost terrace implies that uplift occurred but ended by the Late Pleistocene. However, Antonioli et al. (2006), following Ruggieri et al. (1968) and Ruggieri and Unti (1974), related the same fossiliferous deposit, attributed to MIS 5e, to a terrace with a shoreline angle at ~35 m (our T2), which implies Late Pleistocene uplift at 0.25 mm/a.

We found at the Torre Scibiliana site a *Persististrombus* specimen included within the sedimentary section of terrace T1 (Fig. 7A and G). The specimen is heavily eroded suggesting that it was displaced from a higher terrace. The finding of dislodged *Persististrombus* specimens is not uncommon in the last interglacial terraces in southern Italy (e. g., Nalin et al., 2012), and allows to us to assert that terrace T1 is younger than MIS 5e. This conclusion, coupled to the luminescence age results for the Selinunte Plain transect (Fig. 12), challenges previous attributions and suggests that: 1) terrace T1 formed during MIS 5a; 2) the *Persististrombus* specimen was resedimented within T1 from a higher terrace; 3) the terrace at ~35 m (our T2) is assigned to MIS 5c; 4) terrace T4 formed during MIS 5e.

Antonioli et al. (2006) did not find evidence that the coast east of Capo Granitola experienced Late Pleistocene uplift. They suggested that the poor resistance of the prevailing pelitic rocks therein has led to erosion of any uplifted remain but preferred the alternative view that the MIS 5e terrace is submerged below modern sea level. In this latter scenario, they linked the coastal subsidence to tectonic loading of the Gela Nappe at the frontal thrust system of central Sicily (Figs. 1 and 2A), a sector of recognized Pleistocene tectonic subsidence (Lickorish et al., 1999). The subsidence hypothesis was challenged by Di Maggio et al. (2017), who suggested instead the occurrence of uplift related to crustal thickening and isostatic compensation. However, they calculated a minimal Late Pleistocene uplift (0.032 mm/a) in the area between Marsala and Sciacca, and a much higher rate (0.55 mm/a) east of Sciacca.

In contrast with the existing views, our results indicate that: 1) uplift did not cease by the Late Pleistocene and its rate was significantly higher than previously thought; 2) it occurred along the entire southwestern Sicily coast between Marsala and Capo Bianco, and likely further east as well. We will discuss at length the spatial pattern of uplift in a later section, and focus in this and the following section on its timing and rate.

Results presented here document that uplift occurred along the Selinunte Plain transect, where we assigned the terraces in the flight to specific MISs based on luminescence age constraints, at an average rate of 0.55 mm/a during the last ~400 ka (Table 5; Fig. 14A). Considering that the elevation of terraces continues to increase eastward of this location, we computed the maximum uplift rates along the M. Magaggiaro transect (Fig. 3B). We estimate an average uplift rate of 0.76 mm/a during the last ~313 ka based on displacement of terraces T1-T9 only, because higher terraces are missing (Table 5, Fig. 14A). Both estimates have an uncertainty that decreases with increasing age from ±0.22 (82 ka) to ±0.06 (313 ka) and to ±0.04 (406 ka) (Table 5).

The presence of a staircase of terraces offers the opportunity to calculate uplift rates over specific time intervals. Results for both transect show a variability of incremental uplift rates from ±0.2 to ±0.76 in the Selinunte transect and from ±0.53 to ±1.29 in the Magaggiaro transect (Table 5). Likely, much of this variability is not natural but depends on errors on inner margins and paleo sea-level positioning es-

Table 6
- Chronology of aeolian ridges based on luminescence age constraints and on the genetic relation with dated marine terraces.

Dune order	Dune toe elevation (m)		Age attribution		
	Western sector	Central sector (Selinunte Plain)	Luminescence age constrain	Stratigraphic relation	MIS
D9	–	195–225	–	grown on T11 (MIS 11c) terrace	11a-10
D8	–	165–200	–	grown on T10 (MIS 9e) terrace & T9 (MIS 9c) riser	9b-9d
D7a	155–160	150–175	242 ± 9 (SEL08)	grown on T8 (MIS 9a) riser	8c
D7b	145–150	135–145	–	grown on T8 (MIS 9a) terrace	8a
D6	110	110–120	–	grown on T7 (MIS 7e) terrace	7d
D5	110	100–115	–	grown on T6 (MIS 7c) deposits	7c-7b
D4	60–75	70–80	145 ± 11 (SEL06)	grown on T3 (MIS 6d) terrace and on T5 (MIS 7a) deposits	7a-6
D3a	60	60–65	–	grown on T4 (MIS 5e) riser	5e-5d
D3b	35	30–35	118 ± 9 (SEL09)	grown on T4 (MIS 5e) terrace	5d
D2	20–25	25–30	–	grown on T2 (MIS 5c) riser	5b
D1	10–15	–	–	grown on T1 (MIS 5a) riser	4

timates, as reflected in relatively high uncertainties in incremental uplift rates (Table 5). When uncertainties in uplift estimates are considered, the net trajectory of uplift would be likely be straighter and more aligned to the average trend (Fig. 14A).

6.2. Long-term uplift history

To assess the timing of uplift at longer timescales we compare the maximum displacement of Middle-Late Pleistocene terraces T1 to T11 with indicators of older paleoshorelines provided by higher abrasion surfaces and marine deposits. We develop this issue in the sector of maximum elevation of the terraces, broadly coinciding with the M. Magaggiaro culmination (Fig. 3B).

The Lower Pleistocene (Emilian p. p.-Sicilian substages, ~1.5–0.8 Ma; Di Maggio et al., 2017) Marsala Calcarenite forms a prograding bioclastic carbonate succession that blankets the shore and shelf of western Sicily (Fig. 2A). The succession includes stacked para-sequences of offlapping clinoforms consisting of topsets, foresets and bottomsets that pinch out landward and seaward. The stepped, seaward-dipping erosional surface that levels out the clinoforms represents a composite and time-transgressive toplap surface that was formerly grouped into a single abrasion surface, the GTS (Ruggieri and Unti, 1974), dated to the beginning of the Middle Pleistocene (MIS 17, ~700 ka; D'Angelo and Vernuccio, 1996). Because the GTS is best recognized as a polycyclic surface (Ruggieri and Unti, 1974; Di Maggio et al., 2017), the age of different segments is predicted to scale with their elevation. Indeed, the abrasion surfaces that are found below 200–300 m elevation are associated in our view to Middle Pleistocene terraces that reworked the previous toplap surfaces (Fig. 3C).

The highest toplap surface of the Marsala Calcarenite, where it converges up-dip with the basal onlap surface and marks the oldest preserved outcrops of this formation, lay in the M. Magaggiaro sector at ~280 m elevation. Even allowing a ~30 m paleobathymetry correction for the depth of the toplap surface, we estimate null or minimal (0.04 mm/a) uplift rates between ~1.5–0.4 Ma (Fig. 14B). A relative tectonic quiescence during Emilian-Sicilian is consistent with development of the continuous prograding calcarenite body and with development of the inner part of the GTS above it. Although these estimates have to be considered minimum values because of possible erosional removal of older parts of the calcarenite and because of uncertainty on its basal age, the inference of significant tectonic quiescence holds during the time frame during which the calcarenite was deposited and most likely until ~400 ka.

A chronologic gap whose temporal extent is poorly constrained separates the Marsala Calcarenite from older marine calcarenites, sands and pelites of the Agrigento Formation (Lower Pleistocene Santernian substage) that are found north and west of M. Magaggiaro (Fig. 2A). Near Montevago, the Agrigento Formation is represented by < 100 m of pelites and calcarenites, which are bevelled by an abrasion surface at ~400 m elevation (Montevago surface, Fig. 14B; Di Maggio et al., 2017). This surface developed during a proposed regional erosional phase in western Sicily (Di Maggio et al., 2017) and prior to the deposition of the Marsala Calcarenite. The current elevation difference of the Montevago surface and of the Marsala Calcarenite points to the possibility that Late Santernian-Early Emilian uplift may have been high, possibly up to 0.9 mm/a (Fig. 14B).

Higher abrasion remnants are mapped (Antonioli et al., 2006) at elevations of up to ~650 m in the uppermost reaches of the Belice River valley (Highest Abrasion Surface in Fig. 2A). These surfaces level the Upper Pliocene-Lowermost Pleistocene Belice Marnoso-Arenacea Formation and underlying rocks and could track the onset of uplift in the region prior to deposition of the lower-lying Agrigento deposits. Thus, the interval of high uplift rates could have extended back to ~1.8 Ma, the age of the top of the Marnoso-Arenacea Formation (Fig. 14B). The elevation difference between scattered outcrops of this surface from east to west could be cautiously taken to suggest that Earliest Pleistocene uplift was already asymmetric as it was during the Middle Pleistocene (Fig. 2A).

Summarizing, although substantial uncertainties exist on the pre-Middle Pleistocene uplift history, it appears that uplift during the initial part of the Early Pleistocene might have been as high as during the late Middle-Late Pleistocene, and these phases were separated by a ~1 Ma long interval of minimal or null uplift.

The displacement history reconstructed onshore appears consistent with results of marine geophysical investigations offshore this coast. Based on seismic reflection profiles analysis on the shelf between Capo Granitola and Sciacca, Ferranti et al. (2019) documented that growth rate of transpressional folds associated to the Capo Granitola and Sciacca transcurrent fault systems mapped offshore this coast (Fig. 2A) halved respectively from ~0.2 to 0.4 during Pliocene-Earliest Pleistocene to ~0.1–0.2 mm/a afterwards. The limited resolution of seismic profiles in the shallowest reflector packages did not allow the authors to assess the most recent (Mid-Late Pleistocene) deformation. Nonetheless, high-resolution seismic profiles and bathymetry data published by Lodolo et al., 2020 suggest that uplift of the shelf was substantial at least since the Latest Pleistocene. These authors documented that the Sicily Channel sector between Mazara del Vallo and Sciacca was uplifted at 0.6 mm/a after the Last Glacial Maximum, a value matching the uplift rate estimated by us for the late Middle-Late Pleistocene interval.

6.3. Spatial pattern of uplift

Detailed mapping of the terraces documents that Mid-Late Pleistocene uplift is not uniform spatially but changes along the coast according to a bell-shaped pattern culminating on the coastal projection of the M. Magaggiaro anticline (Figs. 3B and 15A).

In the west, the present coastal plain north of Marsala sharply truncates the terraces elevation profile, but published information from the Egadi Islands (Fig. 2A) provides a pinpoint for the western termination of significant uplift. Indeed, the MIS 5e terrace stands at near-eustatic elevation (~8–12.5 m) in the archipelago starting from Levanzo and Favignana islands ~15 km off mainland Sicily (Fig. 15A; Ferranti et al., 2006; Antonioli et al., 2006; 2018). Thus, the Late Pleistocene and by extension the late Middle Pleistocene uplift profile tapers to minimal values within a maximum distance of 15 km westward of Marsala, i.e. 65 km west of the M. Magaggiaro culmination. Although some recent vertical deformation may be present within the archipelago to account for meter-scale difference between Glacial Isostatic Adjustment (GIA)-predicted models and observed position of the MIS 5e shoreline (Antonioli et al., 2018), we regard these deformations as negligible for the sake of our study.

The eastern termination of uplift is not constrained in the present work, because no terrace was found at or close its eustatic elevation in the eastern sector. However, we estimate that uplift extends for up to ~15 km east of the M. Magaggiaro culmination. At Capo Bianco, ~35 km east of the culmination (Figs. 2A and 3B), we traced the MIS 5e terrace at 55 m elevation. Our result is consistent with the work of Vattano (2008), who mapped in this area five shoreline orders at elevation of up to 400 m and assigned the lowermost one (28–55 m) to the MIS 5e. The elevation of the MIS 5e shoreline at Capo Bianco would fit the progressive elevation decrease of the same shoreline, which descends from ~110 m at the M. Magaggiaro culmination. By extrapolating this trend eastward, the MIS 5e shoreline would be at its original eustatic elevation after additional ~20–30 km, implying a near symmetric uplift profile.

Outcrops of the highest toplap surface of the Marsala Calcarenite lay at elevations that increase from west to east from ~30 to 50 m at Favignana Island in the Egadi Archipelago, to ~130 m on the western coast, up to ~280 m at or near the Magaggiaro culmination, and decrease further eastward, mimicking the deformed shape of younger paleo-shorelines (Fig. 3B). Because the present elevation of the highest outcrops of the Marsala Calcarenite has a minimal elevation difference with the inner margin of T11 (Fig. 3B) the calcarenite was largely uplifted during formation of the Middle-Late Pleistocene terraced sequence.

Furthermore, we observe that the longitudinal topographic profile matches fairly well the deformed shape of the Marsala Calcarenite and of the oldest Middle Pleistocene terraces (Figs. 3B and 15A). The topographic profile was constructed following the highest elevation of the Marsala Calcarenite and projecting them onto a N135 striking direction, parallel to the mean strike of the marine terraces inner margin between Capo Lilibeo and Capo Bianco (Fig. 3A). The shape of the topographic profile suggests that the coastal landscape is a result of Mid-to Late Quaternary uplift.

6.4. Regional and local source contribution to uplift

A closer inspection of the elevation profile of the terrace inner margins and of the Marsala Calcarenite reveals that uplift embeds two components with different wavelength and amplitude that give insights into the combined effects of tectonic processes at different spatial scales. Indeed, two short-wavelength, low-amplitude undulations culminating at ~20–25 and 45–50 km, respectively, are separated by a low centered at ~35 km (Fig. 15A). These undulations that we refer to as local, are superimposed on the larger bell-shaped elevation profile, which we label as regional. The undulations have a-wavelengths, defined as the hinge distance from one culmination to the next, on the order of ~10 km (Fig. 15A). The local undulations are also found in the Marsala Calcarenite, supporting the notion that the calcarenite was deformed during the Middle-Late Pleistocene.

The regional profile instead, as discussed above, has a half-wavelength, from the pinpoint at the Egadi Island to the M. Magaggiaro culmination, of ~65 km and an inferred ~130 km maximum wavelength. Similar wavelength dimensions for regional and local components to those established here were found in the uplift profile of Middle-Late Pleistocene terraces on the Ionian coastline of northern Calabria by Santoro et al. (2013).

A plausible hypothesis on the origin of the short-wavelength undulations comes from appraisal of structural features mapped in southwestern Sicily. The western undulation spatially coincides with the aggregated Gazzera and Campobello anticlines, which form a faulted anticlinorium cored by the Trapanese pelagic platform carbonates (Figs. 2B and 15A). We do not regard this as a fortuitous coincidence and argue that the two folds deformed the Marsala Calcarenite and continued growing during the Middle-Late Pleistocene, leading to bulging of the terraces. The eastern undulation coincides with the location of the Magaggiaro anticline (Fig. 15A) that represents a south-verging, thrust-ramp related fold in the Saccense Platform carbonates (Fig. 2A and B). Unlike the western folds, the terrace profile follows the Magaggiaro anticline along-strike and thus image its along-axis size. The Magaggiaro anticline together with the shorter-size Sciacca anticline to the south, which is not sampled by our analysis, are viewed as the most recent structures of the Sicilian frontal thrust belt (Fig. 2A; Monaco et al., 1996). According to Monaco et al. (1996), the marine terrace at ~100 m (our T4, MIS 5e) is offset by faults related to the Sciacca anticline. Finally, the low between the two undulations at ~35 km, where the terraces profiles exhibit a sharp drop, corresponds to the CCS (Fig. 15A). As described previously, the CCS is a tectonic scarp that borders to the east the ridge that stretches north from Capo Granitola between the villages of Campobello and Castelvetrano (Fig. 2A) and represents the frontal limb of the Campobello anticline (Fig. 2A). According to Barreca et al. (2014; 2020), the scarp is associated to archeoseismic and geodetic evidence of deformation.

Disentangling the relative contribution to the uplift given by regional and local sources requires the assessment of the differential elevation distribution of the paleoshorelines. To extract the regional signal, we computed a linear regression of the elevation data for the terraces T4 to T8, for which we have a relatively well-distributed number of data points (Fig. 15A). The regression was calculated over a ~50 km long stretch between Marsala and a position slightly eastward of the projected M. Magaggiaro culmination. A linear regression was also carried out through the innermost and most elevated outcrops of the Marsala Calcarenite. We then subtracted from the inner margin elevations the expected values calculated from the equation of the linear regression, obtaining in this way a graph showing the effects of the Gazzera, Campobello and Magaggiaro folds (Fig. 15B).

This analysis highlights a northwestward regional tilt of the coast with a mean gradient that regularly increases with terraces age (see slope values in Fig. 15A), and a tilt rate (gradient of the coastline divided by the terrace age) of $\sim 6 \times 10^{-3}$ m km^{-1} ka^{-1}. Results for the Marsala Calcarenite profile are consistent with those for the older Middle Pleistocene terraces when the 406-ka age of T11 is adopted for the onset of deformation, and indicate that regional uplift had a self-consistent shape.

To compute the displacements accommodated by the local structures, we measured the elevation difference between the regional uplift trend and the inner margin of selected terraces. The residual obtained by subtracting the regional signal to the observed terrace position yields the location, amplitude, and growth rate of local structures. Specifically, the undulation related to the Gazzera anticline stands out in the residual profile of terrace T6 with an amplitude of ~20 m (Fig. 15B), pointing to a growth rate of ~0.1 mm/a. Older terraces do not image the anticline because they have been eroded, and younger terraces probably run at the southern periclinal termination of the fold (Fig. 2A) and thus fail to reproduce its occurrence. The Campobello anticline is not evidenced in the differential elevation profile of terraces and probably its effects are mixed with those of the nearby Gazzera anticline, with which it forms a broad anticlinorium (Fig. 2B). The resid-

ual profiles of terraces T4 to T8 show an eastern asymmetry of the undulation, consistent with the long-term fold vergence (Fig. 2B).

The west to east drop of the terraces inner margins across the CCS is imaged in the differential profiles of all terraces. The residual profiles show the syncline developed in the footwall of the Gazzera-Campobello anticlinorium, with an amplitude of between 15 and 20 m for terraces T5 to T7 (Selinunte Plain syncline, Fig. 15B). By considering the ages of the terraces, these estimations yield a growth rate of 0.07–0.08 mm/a.

Support for the syn-depositional growth of the CCS and of its footwall syncline comes from facies analysis of marine deposits associated with terraces T1 to T5 (last ~200 ka), which show higher energy environments just east of the scarp relative to the regions further west, suggesting the scarp might have fostered a local increase in wave energy (see section 2.1 and Table S1). In addition, the CCS stands across the major change in trend of marine terraces and dunes across the study area. Admittedly, the scarp existed before and during the formation of terraces and dunes and controlled their trend and sedimentary environment.

Finally, the Magaggiaro anticline is imaged by residual profiles of terraces T6 to T8, with an amplitude of ~10–15 m, resulting in a growth rate of ~0.06–0.07 mm/a (Fig. 15B). The residual profiles of terraces T4 and T5 do not evidence the anticline, instead they have negative values along the anticline axis. We believe that this pattern is related to their location in the syncline interposed between the M. Magaggiaro and the Sciacca anticlines (Menfi syncline, Fig. 2A and B).

By considering the average uplift rate calculated for the Selinunte Plain and the Magaggiaro transects (Table 5), the ratio of the vertical deformation accommodated by folds in the western (Gazzera-Campobello anticlines and Selinunte Plain syncline) and central (Magaggiaro anticline) sectors is estimated at 15% and 10% of the total uplift, respectively. The remaining displacement ensues from the regional process. These results are consistent with the ratio between fold growth and regional displacement estimated from analysis of uplifted marine terraces in the Ionian side of northern Calabria (Santoro et al., 2013).

The folds outlined by the displacement of the terraces show a clear spatial coincidence with differential deformations revealed by Synthetic Aperture Radar (SAR) Interferometric observations (Barreca et al., 2014). To outline this coincidence, we projected on the terrace profile the Line Of Sight (LOS) mean velocity (Fig. 15B) from SAR data redrawn from Barreca et al. (2014). The SAR profile is sub-parallel (Fig. 2A) to the longitudinal terrace profile. The interferometry data were obtained with the A-DInSAR StaMPS method (Stanford Method for Persistent Scatterers, Hooper, 2008), using image data from the ESA ENVISAT satellite spanning the time period 2003–2010. Although LOS velocities may be affected by non-tectonic amplifications that preclude comparison with uplift rates provided by terraces, the SAR profile, exhibits peaks that coincide with the location of the Gazzera, Campobello and Magaggiaro anticlines and nicely reproduces the current activity of these folds that we argue have caused displacement of Middle-Late Pleistocene terraces (Fig. 15B). The SAR profile also highlights the eastward asymmetry of the Gazzera and Campobello anticlines, consistent with the residual profiles of terraces and with geological reconstructions. Finally, the SAR profile reveals the sharp offset across the CCS and the low coinciding with the Selinunte Plain syncline (Fig. 15B).

6.5. Significance of the regional uplift

In contrast to the deformation accommodated by folds, the regional uplift hints at larger scale processes that in our opinion are shared by the whole front of the Sicilian thrust belt. Late Quaternary uplift rates in excess of 1 mm/a are documented in northeastern Sicily and in Calabria (Ferranti et al., 2006, and references therein), where they are related to residual subduction of the Ionian oceanic slab and concurrent asthenosphere inflow (e. g. Westaway, 1993; Ferranti et al., 2010; Faccenna et al., 2011). Although in the remaining part of Sicily uplift rates outlined by displacement of the MIS 5e terrace are lower, the lack of recognition of significant uplift at the front of the thrust belt in western Sicily so far contrasts with the pattern observed in the eastern part of the island (Fig. 1).

Results of the present study help bridging this gap. We argue that the regional uplift results from continental indentation between the fold and thrust belt and thicker crustal sections of the Pelagian Foreland (Fig. 1). We suspect that the involvement of thick Mesozoic carbonate successions of the Saccense platform at the collision front in western Sicily is the cause for large uplift. Indeed, the culmination of the regional uplift profile in the Sciacca area and its progressive decrease east and west from there possibly reflects the position of the thicker part of the platform which passes laterally to thinner pelagic carbonate platform (PCP) domains (Basilone, 2020, and references therein). Although the exact subsurface transition between the two crustal domains is unknown, the Gazzera-Campobello anticlinorium is likely cored by the Trapanese PCP bedrock, in contrast with the Magaggiaro-Pizzo Telegrafo and Sciacca anticlines that are developed in the Saccense carbonate platform bedrock.

The situation portrayed in western Sicily is akin to what occurs in eastern Sicily, where the thrust belt impinges upon the similarly thick Hyblean carbonate platform. Not surprisingly, the uplift rate inferred since the Last Interglacial at the thrust front in eastern Sicily is ~0.6–0.8 mm/a (Fig. 1), a value similar to that estimated here for the western Sicily front during the last ~400 ka (Fig. 15A). This reconstruction supports the contention that active shortening characterizes the entire front of the SFTB and may be accommodated by steep thrust ramps (Fig. 2B; Lavecchia et al., 2007; Ferranti et al., 2008; Visini et al., 2010).

7. Conclusions

Staircases of marine terraces between ~5 and 250 m elevation in southwestern Sicily document that uplift has occurred in this region, which displays seismic and geodetic evidence of deformation but lacks a detailed seismotectonic model.

Although in the area the morphological signature of the terrace flights is more subdued than in crustal sectors of high uplift rate in southern Italy, like the Calabrian Arc, our detailed mapping constrains the existence of twelve marine terraces whose elevation profile parallel to the coast shows a bell-shaped, near symmetric pattern for a length of ~80 km and probably up to ~130 km.

Luminescence dating of terraced beach barrier ridges and extrapolation of sample uplift rates to undated terraces document that the flight formed during Middle-Late Pleistocene (400 ka) highstands and subordinately interstadial stillstands of the global sea-level curve. In contrast with previous views, our results indicate that displacement has occurred at a fast rate that culminates at average values of 0.75 mm/a in the central part of the uplifted region.

Aeolian ridges that run sub-parallel and are spatially associated to the inner margin of terraces have luminescence ages that document their formation during eustatic lowstands. The aeolian ridges formed as obstacle dunes overlaying a previous inner margin during the regression that followed formation of the underlying terrace. Luminescence ages of aeolian deposits integrated with the proposed model of their formation additionally constrain the chronology of marine terraces.

A closer look at the terrace elevation profile suggests that displacement of terraces embeds both a regional and a local component. The local source reflects active growth of bedrock folds with a half-wavelength of ~10 km and growth rates of up to ~0.1 mm/a, which accounts for ~10–15% of the total uplift. The folds detected in the terraces profile spatially coincide with undulations retrieved in published SAR interferometric data.

The regional component has a vertical tectonic rate similar to the one determined at the collisional front in eastern Sicily. This consistency supports the contention that the Sicily thrust belt is active along

its whole front. Development of these 100-km scale uplift regions is likely related to continental collision between the thrust belt and thick crustal portions (Saccense and Hyblean carbonate platform domains) of the Pelagian foreland of the north African continental margin.

The marine terraces formed above the Early Pleistocene (1.5–0.8 Ma) Marsala Calcarenite that was deposited during a period of relative tectonic quiescence. Remnants of abrasion surfaces carved in progressively higher and older Pleistocene and Late Pliocene rocks suggest that uplift also occurred in the first part of the Pleistocene at rates similar to those estimated for the Middle-Late Pleistocene interval, pointing to alternation of rapid uplift with substantial quiescence.

Analysis of uplifted terraces provides a link between bedrock structures and current geodetic deformation and contributes to bridge the gap between long-term and recent coastal tectonics. The present study highlights the capability of integrated high-resolution mapping and luminescence geo-chronology in detecting pattern and rates of coastal tectonics and in contributing to test geodynamic models and mitigate coastal geo-hazards.

Declaration of competing interest

The authors declare that they have no known competing financial interests or personal relationships that could have appeared to influence the work reported in this paper.

Acknowledgments

This research was supported by funds from INGV-CT granted to Mario Mattia (Progetto Struttura Terremoti: Tettonica attiva in Sicilia sud-occidentale), from the University of Naples funds granted to LF, and from INGV-Rome funds granted to PB. Financial support to SA, VP and DS was provided by a grant from Regione Autonoma Sardegna: L.R. 7/2007, Bando 2017 - Cambiamenti climatici e neotettonica – la Sardegna un continente semi-stabile (P.I. V. Pascucci). Partial funding to VP has been provided by Fondo di Ateneo per la Ricerca 2020, and by the Russian Government Program of Competitive Growth of Kazan Federal University.

Appendix A. Supplementary data

Supplementary data to this article can be found online at https://doi.org/10.1016/j.quascirev.2021.106812.

Data availability

Additional data related to this paper are available by contacting the corresponding author (luigi.ferranti@unina.it).

Author contribution

Ferranti Luigi: Conceptualization, Supervision, Investigation, Writing – original draft, Writing- Reviewing and Editing. Burrato Pierfrancesco: Conceptualization, Investigation, Writing- Reviewing and Editing. Sechi Daniele: Formal analysis, Writing- Reviewing and Editing. Andreucci Stefano: Formal analysis, Writing- Reviewing and Editing. Pepe Fabrizio: Investigation, Writing- Reviewing and Editing. Pascucci Vincenzo: InvestigationFormal Formal analysis, Writing- Reviewing and Editing

References

Andreucci, S., Clemmensen, L.B., Pascucci, V., 2010. Transgressive dune formation along a cliffed coast at 75 ka in Sardinia, West Mediterranean: a record of sea-level fall and increased windiness. Terra. Nova 22, 424–433.

Andreucci, S., Panzeri, L., Martini, I.P., Maspero, F., Martini, M., Pascucci, V., 2014. Evolution and architecture of a west Mediterranean upper Pleistocene to Holocene coastal apron-fan system. Sedimentology 61, 333–361.

Andreucci, S., Sechi, D., Buylaert, J.P., Sanna, L., Pascucci, V., 2017. Post-IR IRSL290 dating of K-rich feldspar sand grains in a wind-dominated system on Sardinia. Mar. Petrol. Geol. 87, 91–98.

Antonioli, F., Kershaw, S., Renda, P., Rust, D., Belluomini, G., Cerasoli, M., Radtke, U., Silenzi, S., 2006. Elevation of the last interglacial highstand in Sicily (Italy): a benchmark of coastal tectonics. Quat. Int. 145–146, 3–18.

Antonioli, F., Ferranti, L., Deiana, G., Lo Presti, V., Furlani, S., Marino, C., Orrù, P., Scicchitano, G., Trainito, E., Anzidei, M., Bonamini, M., Sansò, P., Mastronuzzi, G., 2018. Morphometry and elevation of the last interglacial tidal notches in tectonically stable coasts of the Mediterranean Sea. Earth Sci. Rev. 185, 600–623. doi:10.1016/j.earscirev.2018.06.017.

Armijo, R., Meyer, B., King, G., Rigo, A., Papanastassiou, D., 1996. Quaternary evolution of the Corinth rift and its implications for the late Cenozoic evolution of the Aegean. Geophys. J. Int. 126/1, 11–53. https://doi: 10.1111/j.1365 -246X.1996.tb05264.x.

Auclair, M., Lamothe, M., Huot, S., 2003. Measurement of anomalous fading for feldspar IRSL using SAR. Radiat. Meas. 37, 487–492. doi:10.1016/S1350-4487(03)00018-0.

Azzaro, R., Barbano, M.S., Tertulliani, A., Pirrotta, C., 2020. A reappraisal of the 1968 Valle del Belìce seismic sequence (western Sicily): a case study of intensity assessment with cumulated damage effects. Annals df Geophysics 63 (1). doi:10.4401/ag-8308.

Barreca, G., Bruno, V., Cocorullo, C., Cultrera, F., Ferranti, L., Guglielmino, F., Guzzetta, L., Mattia, M., Monaco, C., Pepe, F., 2014. Geodetic, geological and geophysical evidence of active tectonics in south-western Sicily and offshore. J. Geodyn. 82, 138–149. doi:10.1016/j.jog.2014.03.004.

Barreca, G., Bruno, V., Dardanelli, G., Guglielmino, F., Lo Brutto, M., Mattia, M., Pipitone, C., Rossi, M., 2020. An integrated geodetic and InSAR technique for the monitoring and detection of active faulting in southwestern Sicily. Annals df Geophysics 63 (1). doi:10.4401/ag-8327.

Basilone, L., 2020. Mesozoic tectono-sedimentary evolution of the Trapanese Southern Tethyan margin (NW Sicily) integrating facies and stratigraphic analysis with subsidence history. Italian Journal Geosciences 139 (1), 54–75.

Bateman, M.D., 2015. The application of luminescence dating in sea-level studies. In: Shennan, I., Long, A.J., Horton, B.P. (Eds.), Handbook of Sea-Level Research. John Wiley & Sons, Oxford, pp. 404–417.

Bello, M., Franchino, A., Merlini, S., 2000. Structural model of eastern sicily. Memorie Società Geologica Italiana 55, 61–70.

Bordoni, P., Valensise, G., 1998. Deformation of the 125 ka marine terraces in Italy: tectonic implications. In: Stewart, I., Vita-Finzi, C. (Eds.), Coastal Tectonics, 146. Geol. Soc. London Spec. Publ., pp. 71–110.

Bottari, C., Stiros, S.C., Teramo, A., 2009. Archaeological evidence for destructive earthquakes in sicily between 400 B.C. And A.D. 600. Geoarchaeology 24 (2), 147–175. doi:10.1002/gea.20260.

Bøtter-Jensen, L., Mejdahl, V., 1988. Assessment of beta dose-rate using a GM multicounter system. Int. J. Radiat. Appl. Instrum. Nucl. Tracks Radiat. Meas. 14 (1), 187–191. doi:10.1016/1359-0189(88)90062-3.

Bøtter-Jensen, L., Thomsen, K.J., Jain, M., 2010. Review of optically stimulated luminescence (OSL) instrumental developments for retrospective dosimetry. Radiat. Meas. 45, 253–257.

Buylaert, J.-P., Jain, M., Murray, A.S., Thomsen, K.J., Thiel, C., Sohbati, R., 2012. A robust feldspar luminescence dating method for Middle and Late Pleistocene sediments. Boreas 41, 435–451.

Buylaert, J.P., Murray, A.S., Thomsen, K.J., Jain, M., 2009. Testing the potential of an elevated temperature IRSL signal from K-feldspar. Radiat. Meas. 44, 560–565.

Carr, A.S., Hay, A.S., Powell, D.M., Livingstone, I., 2018. Testing post-IR IRSL luminescence dating methods in the southwest Mojave Desert, California, USA. Quat. Geochronol. 49, 85–91.

Casini, L., Andreucci, S., Sechi, D., Huang, C.-Y., Shen, C.-C., Pascucci, V., 2020. Luminescence dating of Late Pleistocene faults as evidence of uplift and active tectonics in Sardinia. W Mediterranean Terra Nova 32 (4), 261–271. doi:10.1111/TER.12458.

Catalano, R., Franchino, A., Merlini, S., Sulli, A., 2000. Central Western Sicily structural setting interpreted from seismic reflection profiles. Memorie Società Geologica Italiana 55, 5–16.

Catalano, R., Valenti, V., Albanese, C., Accaino, F., Sulli, A., Tinivella, U., Gasparo Morticelli, M., Zanolla, C., Giustiniani, M., 2013. Sicily's fold-thrust belt and slab roll-back: the SI.RI.PRO. seismic crustal transect. J. Geol. Soc. London 170 (3), 451–464.

Chiarella, D., Longhitano, S.G., Tropeano, M., 2017. Types of mixing and heterogeneities in siliciclastic-carbonate sediments. Mar. Petrol. Geol. 88, 617–627. doi:10.1016/j.marpetgeo.2017.09.010.

Civile, D., Lodolo, E., Accaino, F., Geletti, R., Schiattarella, M., Giustiniani, M., Fedorik, J., Zecchin, M., Zampa, L., 2018. Capo Granitola-Sciacca Fault Zone (Sicilian Channel, Central Mediterranean): Structure vs Magmatism. Marine and Petroleum Geology. doi:10.1016/j.marpetgeo.2018.05.016.

Colarossi, D., Duller, G.A.T., Roberts, H.M., 2018. Exploring the behaviour of luminescence signals from feldspars: implications for the single aliquot regenerative dose protocol. Radiat. Meas. 109, 34–44.

Cunningham, A.C., Wallinga, J., 2010. Selection of integration time intervals for quartz OSL decay curves. Quat. Geochronol. 5, 657–666.

Cunningham, A.C., Murray, A.S., Armitage, S.J., Autzen, M., 2018. High-precision natural dose rate estimates through beta counting. Radiat. Meas. 120, 209–214.

de Gelder, G., Jara-Muñoz, J., Melnick, D., Fernández-Blanco, D., Rouby, H., Pedoja, K., Husson, L., Armijo, R., Lacassin, R., 2020. How do sea-level curves influence modeled marine terrace sequences? Quat. Sci. Rev. 229, 106132. doi:10.1016/j.quascirev.2019.106132.

Di Maggio, C., Agate, M., Contino, A., Basilone, L., Catalano, R., 2009. Unconformity-bounded stratigraphic units of Quaternary deposits mapped for the CARG Project in northern and western Sicily. Il Quat. 22 (2), 345–364.

Di Maggio, C., Madonia, G., Vattano, M., Agnesi, V., Monteleone, S., 2017. Geomorphological evolution of western Sicily, Italy. Geol. Carpathica 68 (1), 80–93.

Di Stefano, P., Vitale, F.P., 1993. Carta Geologica dei Monti Sicani Occidentali. Printed by: Università di Palermo, Dipartimento di Geologia e Geodesia. Pezzino, Palermo.

Duller, G.A.T., 2003. Distinguishing quartz and feldspar in single grain luminescence measurements. Radiat. Meas. 37, 161–165.

D'Agostino, N., Selvaggi, G., 2004. Crustal motion along the eurasia-nubia plate boundary in the Calabrian Arc and sicily and active extension in the messina straits from GPS measurements. J. Geophys. Res. 109, B11402.

D'Angelo, U., Vernuccio, S., 1996. I terrazzi marini quaternari della estremità occidentale della Sicilia. Memorie Societa` Geologica Italiana 51, 585–594.

Elshazly, A., Pascucci, V., Khamis, M., 2019. Sedimentary depositional and diagenetic model of a Pleistocene/Holocene coastal formation in Alexandria, Mediterranean Sea, Egypt. J. Afr. Earth Sci. 158. doi:10.1016/j.jafrearsci.2019.103552.

Faccenna, C., Becker, T.W., Lucente, F.P., Jolivet, L., Rossetti, F., 2001. History of subduction and back-arc extension in the Central Mediterranean. Geophys. J. Int. 145, 809–820.

Faccenna, C., Molin, P., Orecchio, B., Olivetti, V., Bellier, O., Funiciello, F., Minelli, L., Piromallo, C., Billi, A., 2011. Topography of the Calabria subduction zone (southern Italy): clues for the origin of Mt. Etna. Tectonics 30, TC1003 http://doi.org/10. 1029/2010TC002694.

Fedorik, J., Toscani, G., Lodolo, E., Civile, D., Bonini, L., Seno, S., 2017. Structural analysis and miocene-to-present tectonic evolution of a lithospheric-scale, transcurrent lineament: the Sciacca Fault (Sicilian channel, central Mediterranean Sea). Tectonophysics 722, 342–355.

Ferranti, L., Antonioli, F., Mauz, B., Amorosi, A., Dai Prà, G., Mastronuzzi, G., Monaco, C., Orru', P., Pappalardo, M., Radtke, U., Renda, P., Romano, P., Sansò, P., Verrubbi, V., 2006. Markers of the last interglacial sea level high stand along the coast of Italy: tectonic implications. Quat. Int. 145–146, 30–54. doi:10.1016/j.quaint.2005.07.009.

Ferranti, L., Oldow, J.S., D'Argenio, B., Catalano, R., Lewis, D., Marsella, E., Avellone, G., Maschio, L., Pappone, G., Pepe, F., Sulli, A., 2008. Active deformation in southern Italy, sicily and southern sardinia from GPS velocities of the peri-tyrrhenian geodetic array (PTGA). Bollettino Società Geologica Italiana 127, 299–316.

Ferranti, L., Santoro, E., Mazzella, M.E., Monaco, C., Morelli, D., 2009. Active transpression in the northern Calabria Apennines, southern Italy. Tectonophysics 476, 226–251. doi:10.1016/j.tecto.2008.11.010.

Ferranti, L., Antonioli, F., Anzidei, M., Monaco, C., Stocchi, P., 2010. The timescale and spatial extent of vertical tectonic motions in Italy: insights from relative sea-level changes studies. J. Virtual Explor. 36, 1–34. doi:10.3809/jvirtex.2009.00255.

Ferranti, L., Pepe, F., Barreca, G., Meccariello, M., Monaco, C., 2019. Multi-temporal tectonic evolution of Capo Granitola and Sciacca foreland transcurrent faults (Sicily channel). Tectonophysics 765, 187–204. doi:10.1016/j.tecto.2019.05.002.

Fornós, J., Clemmensen, L.B., Gomez-Pujol, L., Murray, A.S., 2009. Late Pleistocene carbonate aeolianite deposits on Mallorca, western Mediterranean: a luminescence chronology. Quat. Sci. Rev. 28, 2697–2709.

Ghisetti, F.C., Gorman, A.R., Grasso, M., Vezzani, L., 2009. Imprint of foreland structure on the deformation of a thrust sheet: the Plio-Pleistocene Gela Nappe (southern Sicily, Italy). Tectonics 28 (4).

Guérin, G., Mercier, N., Adamiec, C., 2011. Dose-rate conversion factors: update. Ancient TL 29, 5–8.

Guérin, G., Mercier, N., Nathan, R., Adamiec, G., Lefrais, Y., 2012. On the use of the infinite matrix assumption and associated concepts: a critical review. Radiat. Meas. 47 (9), 778–785.

Guidoboni, E., Muggia, A., Marconi, C., Boschi, E., 2002. A case study in archaeoseismology. The collapses of the Selinunte temples (Southwestern Sicily): two earthquakes identified. Bull. Seismol. Soc. Am. 92 (8), 2961–2982. doi:10.1785/0120010286.

Gurrola, L.D., Keller, E.A., Chen, J.H., Owen, L.A., Spencer, J.Q., 2014. Tectonic geomorphology of marine terraces: santa Barbara fold belt, California. Geol. Soc. Am. Bull. 126 (1–2), 219–233. https://doi: 10.1130/B30211.1.

Hamon-Kerivel, K., Cooper, A., Jackson, D., Sedrati, M., Pintado, E.G., 2020. Shoreface mesoscale morphodynamics: a review. Earth Sci. Rev. 209, 103330.

Huntley, D.J., Baril, M.R., 1997. The K content of the K-feldspars being measured in optical dating or in thermoluminescence dating. Ancient TL 15, 11–13.

Huntley, D.J., Lamothe, M., 2001. Ubiquity of anomalous fading in K-feldspars and the measurement and correction for it in optical dating. Can. J. Earth Sci. 38, 1093–1106.

Jara-Muñoz, J., Melnick, D., Brill, D., Strecker, M.R., 2015. Segmentation of the 2010 Maule Chile earthquake rupture from a joint analysis of uplifted marine terraces and seismic-cycle deformation patterns. Quat. Sci. Rev. 113, 171–192.

Kars, R.H., Reimann, T., Wallinga, J., 2014. Are feldspar SAR protocols appropriate for post-IR IRSL dating? Quat. Geochronol. 22, 126–136.

Lavecchia, G., Ferrarini, F., de Nardis, R., Visini, F., Barbano, S., 2007. Active thrusting as a possible seismogenic source in Sicily (Southern Italy): some insights from integrated structural-kinematic and seismological data. Tectonophysics 445, 145–167.

Lentini, F., Carbone, S., 2014. Geological Map of Sicily, Scale 1:250.000. SELCA, Firenze. www.selca-cartografie.it.

Li, B., Jacobs, Z., Roberts, R.G., Li, S.-H., 2014. Review and assessment of the potential of post-IR IRSL dating methods to circumvent the problem of anomalous fading in feldspar luminescence. Geochronometria 41, 178–201.

Lickorish, W.H., Grasso, M., Butler, R.W.H., Argnani, A., Maniscalco, R., 1999. Structural styles and regional tectonic setting of the "Gela Nappe" and frontal part of the Maghrebian thrust belt in Sicily. Tectonics 18, 655–668.

Lodolo, E., Galassi, G., Spada, G., Zecchin, M., Civile, D., Bressoux, M., 2020. Post-LGM coastline evolution of the NW Sicilian Channel: comparing high-resolution geophysical data with Glacial Isostatic Adjustment modeling. PloS One 15 (2), e0228087. doi:10.1371/journal.pone.0228087.

Lui, J., Murray, A.S., Sohbati, R., Jain, M., 2016. The effect of test dose and first IR stimulation temperature on post-IR IRSL measurements of rock slices. Geochronometria 43, 179–187.

Malinverno, A., Cafiero, M., Ryan, W.B.F., Cita, M.B., 1981. Distribution of Messinian sediments and erosional surfaces beneath the Tyrrhenian sea-geodynamic implications. Oceanol. Acta 4 (4), 489–495.

Miyauchi, T., Dai Pra, G., Sylos Labini, S., 1994. Geochronology of Pleistocene marine terraces and regional tectonics in tyrrhenian coast of south Calabria, Italy. Il quaternario. Italian Journal of Quaternary Sciences 7, 17–34.

Monaco, C., Mazzoli, S., Tortorici, L., 1996. Active thrust tectonics in western Sicily (southern Italy): the 1968 Belice earthquake sequence. Terra. Nova 8 (4), 372–381.

Montanari, D., Minissale, A., Doveri, M., Gola, G., Trumpy, E., Santilano, A., Manzella, A., 2017. Geothermal resources within carbonate reservoirs in western Sicily (Italy): a review. Earth Sci. Rev. 169, 180–201.

Muhs, D.R., Simmons, K.R., Schumann, R.R., Groves, L.T., DeVogel, S.B., Minor, S.A., Laurel, D., 2014. Coastal tectonics on the eastern margin of the pacific rim: late quaternary sea-level history and uplift rates, channel islands national park, California, USA. Quat. Sci. Rev. 105, 209–238. https://doi: 10 .1016/j.quascirev.2014.09.017.

Murray, A.S., Wintle, A.G., 2000. Luminescence dating of quartz using an improved single-aliquot regenerative-dose protocol. Radiat. Meas. 32, 57–73.

Murray, A.S., Wintle, A.G., 2003. The single aliquot regenerative dose protocol: potential for improvements in reliability. Radiat. Meas. 37, 377–381.

Nalin, R., Bracchi, V.A., Basso, D., Massari, F., 2012. *Persististrombus latus* (GMELIN) in the upper Pleistocene deposits of the marine terraces of the Crotone peninsula (southern Italy). Italian Journal of Geosciences 131, 95–101.

Nielsen, K.A., Clemmensen, L.B., Fornós, J.J., 2004. Middle Pleistocene magnetostratigraphy and susceptibility stratigraphy: data from a carbonate aeolian system, Mallorca, Western Mediterranean. Quat. Sci. Rev. 23, 1733–1756.

Pascucci, V., Sechi, D., Andreucci, S., 2014. Middle Pleistocene to holocene coastal evolution of NW sardinia (Mediterranean Sea, Italy). Quat. Int. 328–329, 3–20.

Pascucci, V., De Falco, G., Del Vais, C., Melis, R., Sanna, I., Andreucci, S., 2018. Climate changes and human impact on the mistras coastal barrier system (W sardinia, Italy). Mar. Geol. 395, 271–284. doi:10.1016/j.margeo.2017.11.002.

Pascucci, V., Frulio, G., Andreucci, S., 2019. New estimation of the post little ice age relative sea-level rise. Geosciences 9, 348. doi:10.3390/geosciences9080348.

Plafker, G., Rubin, M., 1978. Uplift history and earthquake recurrence as deduced from marine terraces on middleton island, Alaska. U.S. Geological Survey Open-File Report 687–721.

Porat, N., Faerstein, G., Medialdea, A., Murray, A.S., 2015. Re-examination of common extraction and purification methods of quartz and feldspar for luminescence dating. Ancient TL 33 (1), 22–30.

Prescott, J.R., Hutton, J.T., 1994. Cosmic ray contributions to dose rates for luminescence and ESR dating: large depths and long-term time variations. Radiat. Meas. 23, 497–500.

Railsback, L.B., Gibbard, P.L., Head, M.J., Voarintsoa, N.R.G., Toucanne, S., 2015. An optimized scheme of lettered marine isotope substages for the last 1.0 million years, and the climatostratigraphic nature of isotope stages and substages. Quat. Sci. Rev. 111, 94–106. doi:10.1016/j.quascirev.2015.01.012.

Roberts, H.M., 2006. Optical dating of coarse-silt sized quartz from loess: evaluation of equivalent dose determinations and SAR procedural checks. Radiat. Meas. 41, 923–929.

Roure, F., Howell, D.G., Moretti, I., Müller, C., 1990. Neogene subduction complex of Sicily. J. Struct. Geol. 12, 259–266. doi:10.1016/0191-8141(90)90009-N.

Ruggieri, G., Unti, M., 1974. Pliocene e Pleistocene nell'entroterra di Marsala. Bollettino Società Geologica Italiana 93, 723–733.

Rovida, A., Locati, M., Camassi, R., Lolli, B., Gasperini, P., Antonucci, A., 2021. Catalogo Parametrico dei Terremoti Italiani (CPTI15), versione 3.0. Istituto Nazionale di Geofisica e Vulcanologia (INGV). doi.org/10.13127/CPTI/CPTI15.3.

Ruggieri, G., Buccheri, G., Rendina, M., 1968. Segnalazione di Tirreniano fossilifero a trapani. Riv. Mineraria Sicil. 112/11, 1–4.

Ruggieri, G., Unti, A., Unti, M., Moroni, M.A., 1975. La calcarenite di Marsala (Pleistocene Inferiore) e i terreni contermini. Bollettino Società Geologica Italiana 94, 1623–1655.

Santoro, E., Mazzella, E., Ferranti, L., Randisi, E., Napolitano, E., Rittner, S., Radtke, U., 2009. Raised coastal terraces along the Ionian Sea coast of northern Calabria, Italy, suggest space and time variability of tectonic uplift rates. Quat. Int. 206, 78–101. doi:10.1016/j.quaint.2008.10.003.

Santoro, E., Ferranti, L., Burrato, P., Mazzella, M.E., Monaco, C., 2013. Deformed Pleistocene marine terraces along the Ionian Sea margin of southern Italy: unveiling blind fault-related folds contribution to coastal uplift. Tectonics 32, 1–26. doi:10.1002/tect.20036.

Sechi, D., Andreucci, S., Stevens, T., Pascucci, V., (in press). Age and significance of late Pleistocene Lithophyllum byssoides intertidal algal ridge, NW Sardinia, Italy. Sediment. Geol. 400 http://doi.org/10.1016/j.sedgeo.2020.105618.

Shackleton, N.J., 2000. The 100,000-year Ice-Age cycle identified and found to lag temperature, carbon dioxide, and orbital eccentricity. Science 289, 1897–1902.

Sloss, C.R., Shepherd, M., Hesp, P., 2012. Coastal dunes: geomorphology. Nature Education Knowledge 3 (10), 2.

Thiel, C., Coltorti, M., Tsukamoto, S., Frechen, M., 2010. Geochronology for some key sites along the coast of Sardinia (Italy). Quat. Int. 222, 36–47.
Thiel, C., Buylaert, J.P., Murray, A., Terhorst, B., Hofer, I., Tsukamoto, S., Frechen, M., 2011. Luminescence dating of the Stratzing loess profile (Austria)—testing the potential of an elevated temperature post-IR IRSL protocol. Quat. Int. 234, 23–31.
Thomsen, K.J., Murray, A.S., Buylaert, J.-P., Jain, M., Hansen, J.H., Aubry, T., 2016. Testing single-grain quartz OSL methods using sediment samples with independent age control from the Bordes-Fitterockshelter (Rochesd'Abilly site, Central France). Quat. Geochronol. 31, 77–79.
Vattano, M., 2008. Evoluzione geomorfologica di aree carsiche nelle evaporiti della Sicilia centro-meridionale attraverso l'analisi delle relazioni tra forme carsiche ipogee e forme del rilievo di superficie. PhD Thesis. Università degli Studi di Palermo, p. 250.
Visini, F., de Nardis, R., Lavecchia, G., 2010. Rates of active compressional deformation in central Italy and Sicily: evaluation of the seismic budget. Int. J. Earth Sci. 99 (1), S243–S264. doi:10.1007/s00531-009-0473-x.
Vitale, F.P., 1990. Carta geologica ella Valle del medio Belice, scale 1:50.000. In: Vitale, F.P. (Ed.), Studi sulla Valle del medio Belice (Sicilia centro-occidentale). L'avanfossa Plio-Pleistocenica nel quadro dell'evoluzione paleotettonica dell'area. PhD Thesis, Università degli Studi di Palermo. p. 202.
Waelbroeck, C., Labeyrie, L., Michel, E., Duplessy, J.C., Lambeck, K., McManus, J.F., Balbon, E., Labracherie, M., 2002. Sea-level and deep-water temperature changes derived from benthic foraminifera isotopic records. Quat. Sci. Rev. 21, 295–305.
Westaway, R., 1993. Quaternary uplift of southern Italy. J. Geophys. Res. 98, 21741–21772.
Wintle, A.G., Murray, A.S., 2006. A review of quartz optically stimulated luminescence characteristics and their relevance in single-aliquot regeneration dating protocols. Radiat. Meas. 41 (4), 369–391.
Yi, S., Buylaert, J.P., Murray, A.S., Lu, H., Thiel, C., Zeng, L., 2016. A detailed post-IR IRSL dating study of the Niuyangzigou loess site in northeastern China. Boreas 45 (4), 644–657.